Optical spectra of doubly charged quantum dot molecules in electric and magnetic fields

M. F. Doty,* M. Scheibner, A. S. Bracker, I. V. Ponomarev, T. L. Reinecke, and D. Gammon
Naval Research Laboratory, Washington, District of Columbia 20375, USA
(Received 2 June 2008; revised manuscript received 30 July 2008; published 19 September 2008)

We present an experimental and theoretical study of the photoluminescence spectra of individual doubly charged quantum dot molecules. The quantum dot molecules consist of two vertically stacked InAs self-assembled quantum dots in a GaAs Schottky diode structure. We study two cases: (1) the two dots are charged with two electrons coherently coupled through electron tunneling and (2) the two dots are charged with two holes and coherently coupled through hole tunneling. The optically excited states consist of the two charges along with one or two additional electron-hole pairs, i.e., a doubly charged exciton and biexciton. We determine the spin states and the corresponding spectral fine structure and show how this fine structure depends on vertical electric and magnetic fields. We find that the results are in large part qualitatively similar for the two cases. However, when magnetic fields are applied, we find a strong g factor resonance and evidence of a bonding/antibonding reversal for the hole-tunneling case only. We discuss the implications for quantum information processing using spins confined in proximate dots.

DOI: 10.1103/PhysRevB.78.115316 PACS number(s): 78.20.Ls, 78.47.−p, 78.55.Cr, 78.67.Hc

I. INTRODUCTION

The development of devices for spintronics and solid-state quantum information processing has been a primary motivation in condensed-matter physics research over the past decade.[1] Because of their ability to spatially localize single spins, quantum dots (QDs) have been at the forefront of this field. One of the first proposals for the implementation of quantum information processing in solid-state systems was based on gated exchange interactions between spins in two neighboring QDs.[2] Over the years there has been considerable experimental and theoretical progress in the coherent control and interaction of spins in both single and coupled QDs. Single spin manipulations and controllable coupling have been demonstrated in lithographically defined QDs.[3–7] Optically active QDs offer the possibility of using ultrafast laser techniques for initialization, readout, and coherent manipulation of spins.[8–12] Further development of such techniques, particularly for coupled QDs, requires detailed characterization of the Coulomb and spin interactions in both the ground and optically excited states.

The first optical studies of single quantum dot molecules (QDMs) found spectroscopic evidence of coupling between the dots.[13] More detailed studies became possible when the QDMs were embedded into a diode structure that enabled tuning of the relative energy levels of the two dots by an applied electric field.[14,15] In 2006 the spectroscopic signatures of coupling in charged QDMs were identified and it was shown that selective tunneling of either electrons or holes could be engineered.[16,17] Substantial progress has been made in understanding the properties of QDMs,[18–20] including the origins of spin fine structure[21] and the properties of spins delocalized over the entire QDM.[22,23] Techniques have been developed for differential transmission spectroscopy,[24] mapping excited states,[25] and executing conditional quantum dynamics.[26] In parallel, there has been substantial progress in calculating the optical spectra of QDMs.[27–37]

Because of potential applications in solid-state quantum information processing or spin-based logic, the case of two spins confined in a pair of coupled QDs deserves special attention. Some aspects of the spectra of doubly charged QDMs at zero magnetic field have been discussed in previous works.[18,21] In this paper, we present a detailed study of the charge and spin interactions in optically active QDMs charged with two electrons or two holes as a function of both applied electric and magnetic fields. We provide explanations of spin and charge fine structure and discuss how the magnitudes of the underlying interactions can be controlled by sample parameters. Our sample structure and experimental methods are described in Sec. II. In Sec. III we present our method for analyzing coherent tunnel coupling using atomiclike basis states and matrix Hamiltonians. Experimentally observed spectra are presented and large-scale features are explained in Sec. IV. In Sec. V we present the state Hamiltonians, discuss the spin-exchange interactions, and discuss how these interactions depend on the sample structure. In Sec. VI we discuss the application of magnetic fields that introduce Zeeman splittings between orthogonal spin projections and reveal resonant changes in g factor that can be used to electrically modulate spin splitting and identify the orbital character of delocalized molecular states. After a summary in Sec. VII, we discuss the implications of this work for quantum information processing and spin-based logic in Sec. VIII. The Appendix has detailed information on the basis states and the Hamiltonians presented throughout the work.

II. SAMPLE STRUCTURE AND PHOTOLUMINESCENCE MEASUREMENTS

The QDMs we study are grown by the molecular-beam epitaxial deposition of two closely spaced layers of self-assembled InAs/GaAs QDs. The QDs were embedded in the insulating region of n-i or p-i Schottky diodes grown on doped GaAs substrates. Tellurium (from a GaTe source) was used for n-type doping and beryllium for p-type doping. The bottom QD was separated from the doped buffer layer by an 80 nm undoped GaAs layer. After a 2 min growth interruption at 580 °C, the QDs were grown at a substrate tempera-

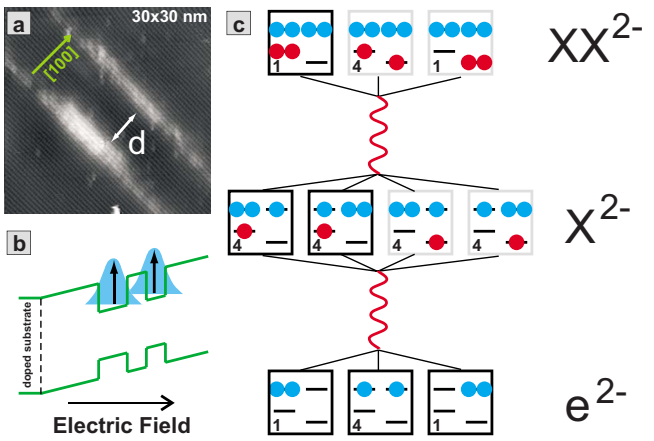

FIG. 1. (Color online) (a) Cross-sectional scanning tunneling microscope image of a QDM; image adapted from Ref. 25. (b) Schematic depiction of the band structure of a quantum dot molecule containing two electron spins with an electric field applied along the [100] direction. (c) Charge configurations of a doubly negatively charged QDM in its ground state (bottom row, e^{2-}), first optical excited state (middle row, X^{2-}), and second optical excited state (top row, XX^{2-}). Electrons and holes are restricted to the lowest-energy levels in each dot. The number of spin configurations is shown in the bottom left corner of each box. The configurations in the gray boxes are considered unstable at electric fields close to the resonance of the electron levels due to fast relaxation of the hole(s).

ture of 520 °C and a growth rate of ~0.04 monolayers/s. Sample rotation was stopped during InAs deposition to produce a large QD density gradient across the wafer. The two layers of dots are separated by a GaAs barrier of thickness d, grown at 530 °C, as shown in the cross-sectional scanning tunneling microscope (XSTM) image of a typical QDM in Fig. 1(a). Strain causes the dots of the second layer to nucleate preferentially on top of the dots in the first layer, thereby forming QDMs.

The vertical height of the QDs is controlled by the application of an indium flush technique: a thin GaAs cap (2–4 nm) was grown over the QDs at 520 °C, followed by a slow ramp and anneal at 580 °C for 100 s.[38,39] This technique creates QDs with a disk shape, as can be seen in Fig. 1(a). The vertical height of the QDs determines the ground-state transition energy. The diode structures were completed above the QDs with GaAs/$Al_{0.7}Ga_{0.3}As$ layers (~280 nm total thickness) to reduce the current. For the *n-i* diodes, a 40 nm AlGaAs layer was grown near the sample surface. For the *p-i* diodes, a 270 nm AlGaAs layer started 2 nm above the QDs in order to inhibit escape of carriers from the QDs. Both types of samples were capped with 10 nm of GaAs to prevent AlGaAs oxidation.

Following growth, low-temperature photoluminescence images of the wafers were obtained to locate the regions of appropriate density for single molecule spectroscopy. A "shadow mask" was used to isolate single QDMs: a semitransparent layer of titanium (5 nm) was deposited on the sample surface followed by a 130 nm layer of aluminum. Electron-beam lithography was used to pattern the aluminum with 1 μm apertures.

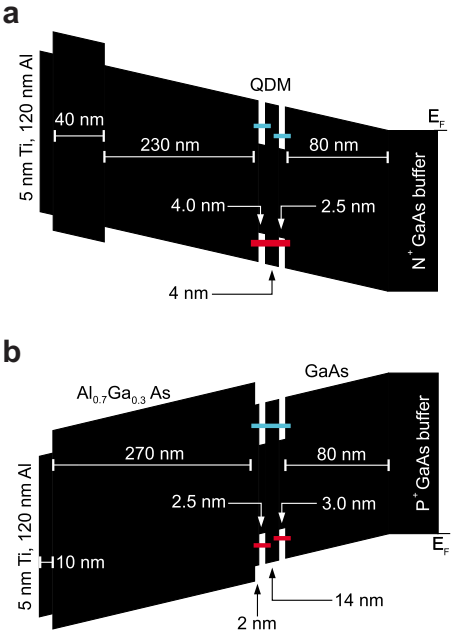

FIG. 2. (Color online) Example sample dimensions for (a) hole tunneling in a sample with $d=4$ nm and (b) electron tunneling in a sample with $d=14$ nm. Schematics are not to scale. We have measured samples with d ranging from 2 to 16 nm.

Even if both dots in a QDM are grown under nominally identical conditions, strain and asymmetry generally lead to nondegenerate dots with slightly different energy levels. The diode structure allows application of an electric field in the direction of the molecular axis [see Fig. 1(b)]. The applied field controls the relative energy levels of the two dots and can be used to tune either electron or hole energy levels into resonance *in situ*. The substrate doping and relative heights of the two dots determine whether electrons or holes tunnel.[17]

For electron tunneling, a *p*-type substrate is used. For hole tunneling, an *n*-type substrate is used. The heights of the dots are chosen such that the bottom dot has a lower confinement energy (i.e., redshifted relative to the top dot). An example of each sample type is shown in Fig. 2. In our QDMs, the additional charges are generated optically. For example, a two-electron ground state is populated when the hole tunnels to the *p*-type substrate before an injected electron-hole pair recombines. Two such tunneling events are required to populate the doubly negatively charged ground state, but the excess electrons then remain confined in the dot until either a free hole tunnels back into the dot or the excess electron tunnels out. This technique allows us to measure the full spectra of several different charge configurations. Growing the QDs far from the underlying doping region enhances this effect. For the case of electron charging (in the *p*-type Schottky diode), the AlGaAs barrier was grown close above the QDs to keep the electrons from tunneling to the surface. Because optical charging is a random process, several different charge states appear simultaneously in our spectra. The particular location of each charge configuration is determined by Coulomb interactions. Specific charge configurations can be identified from their relative locations and spin fine structure as discussed below.[21]

We probe the energy levels of QDMs using photoluminescence. Because ensembles of QDMs have a very large distribution of parameters, resolving charge and spin fine structure requires isolating single QDMs. Individual QDMs were optically excited and detected through an aluminum shadow mask with 1 μm diameter apertures. Excitation was performed with a continuous-wave titanium-sapphire laser tuned to wavelengths between 895 and 930 nm. The laser wavelength is energetically well below the wetting layer emission at about 870 nm. The collected photoluminescence signal was dispersed with a 0.75 m monochromator equipped with an 1100 mm^{-1} line grating and was detected by a liquid-nitrogen-cooled charge coupled device (CCD) camera. The overall spectral resolution is about 70 μeV.

The energy of the emitted photons is determined by the difference in energy between the initial and the final states of the optical recombination. The photoluminescence spectrum of QDMs is recorded as a function of the electric field applied to the diode structure. The individual spectra [photoluminescence (PL) intensity vs energy] are assembled to create a spectral map with energy on one axis, applied electric field on the other axis, and the PL intensity color coded (see Fig. 4).

III. ATOMIC BASIS STATES AND MOLECULAR ORBITALS

In this report we focus on QDMs that are charged with either two electrons or two holes. Figure 1(c) depicts the possible charge configurations for a doubly negatively charged QDM in its optical ground state (e^{2-}), excitonic state (X^{2-}), and biexcitonic state (XX^{2-}). We consider only the lowest confined energy levels for electrons in the conduction band and holes in the valence band of each QD.

In QDMs, there are several possible spatial distributions of charges. We will describe the spatial distribution of charges as $\binom{m_e,n_e}{m_h,n_h}$, where $m_{e(h)}$ and $n_{e(h)}$ indicate the numbers of electrons (holes) in the bottom and top dots, respectively. We will continue to use the excitonic notation to describe the total number of charges in a QDM (i.e., X^{2+} refers to any configuration of one electron and three holes). Coulomb interactions between multiple charges in a QDM shift the relative energy levels of each configuration. These Coulomb interactions are the origin of the characteristic energy shifts for PL lines of excitons in single QDs that contain more than a single electron-hole pair [for example the trion, biexciton, etc.].

We calculate the energy levels of QDMs in a matrix Hamiltonian using atomiclike basis states that are coupled together via tunneling. As an example, we consider two X^{2-} states, neglecting the spin interactions that will be discussed in Sec. V:

$$\hat{H} = \begin{matrix} \binom{2,1}{1,0} & \binom{1,2}{1,0} \end{matrix} \begin{pmatrix} E_0 + \Gamma & t \\ t & E_0 + edF \end{pmatrix}. \quad (1)$$

E_0 is the excitonic energy determined by the electron-hole pair and Γ is an energy shift due to different Coulomb interactions in the two basis states. Because we have chosen the energy of the configuration where each dot is occupied by one electron to be field independent, the energy of the state $\binom{2,1}{1,0}$, which has a *net* charge of one electron per dot, has no dependence on the applied electric field (F). $\binom{1,2}{1,0}$ has a net charge of two electrons in the top dot, and thus edF captures the change in energy with applied electric field.[40] e is the electron charge and the dots are separated by an effective barrier thickness d. The off-diagonal matrix element t is the rate at which electrons tunnel between the two dots. The magnitude of the tunnel coupling depends on the thickness of the barrier between the dots and the relative detuning of the electron energy levels in each dot.

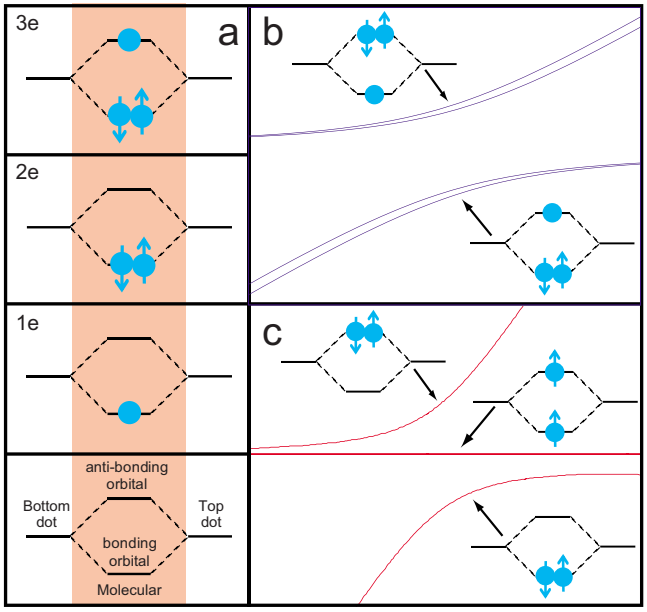

FIG. 3. (Color online) (a) The lowest-energy molecular states in charged QDMs are determined by sequentially filling the orbitals with particles. (b) Delocalized molecular states of X^{2-}, which has three electrons (and one hole; not shown), have different orbital configurations. (c) At an anticrossing of the e^{2-} state, the upper and lower branches have singlet orbital configurations. Only one example of triplet orbital configurations is labeled. Both (b) and (c) plot state energies as a function of applied electric field. The plots are extracted from full calculations of the energy levels similar to those in Fig. 7 and consequently exhibit some fine structure due to spin interactions that are explained in Sec. V.

When energy levels are tuned into resonance, coherent tunnel coupling causes the particles to form molecular orbitals delocalized over both dots and the intervening barrier. The formation of these molecular orbitals results in anticrossings (ACs) in the energy levels as a function of applied electric field.[14] See, for example, Fig. 3(b). The energy difference between the upper and the lower branches is the anticrossing gap. The magnitude of this gap is determined by the degree of tunnel coupling, which is in turn determined by the properties of the barrier between the dots. The substrate doping and relative heights of the two dots can be used to select whether electrons or holes tunnel.[17] Electrons and holes have substantially different tunneling rates due to their different effective masses.[17] In addition, holes have a spin-

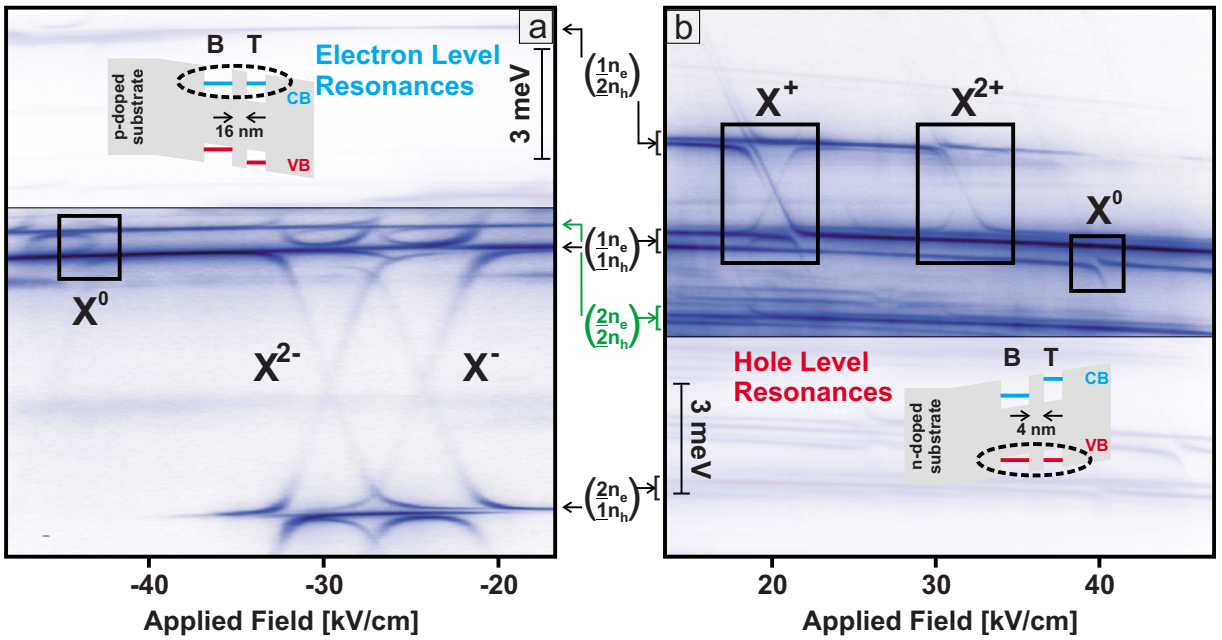

FIG. 4. (Color online) Comparison between the field-dependent spectra of (a) a QDM for which the electron levels are tuned into resonance and (b) a QDM for which the hole levels are tuned into resonance. In both QDMs the bottom dot has a smaller band gap. The QDM in (a) with a dot separation of 16 nm was embedded in a *p*-type Schottky diode structure, whereas the QDM in (b) with a dot separation of 4 nm was embedded in an *n*-type Schottky diode structure. In both spectra the ground-state molecular resonance of the neutral exciton and the x patterns of the singly and doubly charged excitons are marked. A dark rectangle is sometimes used to clearly identify the corresponding spectral features. The labels between panels (a) and (b) indicate X^0-like $\binom{1,n_e}{1,n_h}$, X^+-like $\binom{1,n_e}{2,n_h}$, X^--like $\binom{2,n_e}{1,n_h}$, and XX^0-like $\binom{2,n_e}{2,n_h}$ intradot (single-dot) transitions, where $n_{e(h)}$ is the number of electrons (holes) in the top dot that do not take part in the optical transition. Like all spectral maps presented here, the intensity is displayed on a nonlinear quasilogarithmic scale chosen to reveal weak spectral features without saturating strong features. Note that the shaded area in (b) also shows the X^0 and X^+ PL transitions from a second molecule.

orbit interaction that can substantially change the tunnel coupling.[23]

Our use of atomiclike basis states coupled together via tunneling is similar to the Heitler-London method that can be used to analyze the states of simple diatomic molecules such as H_2.[41] In Eq. (1) the basis states are simply two possible spatial distributions of the particles. Away from resonance (large magnitude of F), the tunnel coupling is minimal and the eigenvalues of Eq. (10) are essentially just the energies of the two basis states. This is the atomiclike or Heitler-London limit. On resonance ($edF=\Gamma$), the eigenvalues of Eq. (1) are $E_0+\Gamma-t$ and $E_0+\Gamma+t$. The eigenstates that correspond to these values are, respectively, the symmetric (bonding) and antisymmetric (antibonding) combination of the two basis states.

An alternative to the Heitler-London approach is to begin with the single-particle eigenstates of the molecule: the bonding and antibonding molecular orbitals.[42] The formation of these molecular orbitals is depicted in the energy diagrams in Fig. 3(a). The ground state of a charged molecule is determined by filling these molecular orbitals with particles beginning with the lowest-energy state, as shown in Fig. 3(a). In Figs. 3(b) and 3(c) we show how these orbital diagrams can be used to label the molecular states at anticrossings in the X^{2-} and e^{2-} states. The fine structure that appears in these anticrossings will be explained in Sec. V. Here we focus only on the formation of delocalized molecular orbitals. Because the applied electric field controls the magnitude of tunnel coupling, the states of QDMs evolve continuously between atomiclike and molecular orbitals as a function of applied electric field.

The molecular-orbital formulation provides important insights into the states of QDMs. For two electrons, the lowest-energy configuration places both electrons in the same orbital state, which requires that they be in a spin singlet. If the spins are in separate orbital states, both singlet and triplet states are possible; we show one possible triplet state in Fig. 3(c). If a third electron is added, the lowest-energy configuration has two electrons in a spin singlet in the bonding orbital, with the remaining electron alone in the antibonding orbital. Note that in Fig. 3 the single-particle bonding orbital has the lowest energy. This is the case when t is positive, as it is for natural molecules. However, when holes tunnel through a relatively thick barrier, spin-orbit interactions can reverse the sign of t and create an antibonding ground state.[23,43]

IV. MEASURED AND CALCULATED PHOTOLUMINESCENCE SPECTRA

In Fig. 4 we present full spectral maps of both positively and negatively charged QDMs. By studying the full spectral map, we can identify the relationship between neutral, singly, and doubly charged excitons and demonstrate that the same concepts apply equally well to QDMs charged with both electrons and holes. We consider two QDMs: a QDM with

16 nm barrier embedded in a p-type diode to obtain electron tunneling [Fig. 4(a)] and a QDM with a 4 nm barrier embedded in an n-type diode to obtain hole tunneling [Fig. 4(b)]. Both spectral bias maps in Fig. 4 span the same energy range. The maps are aligned on the intradot transitions of the neutral exciton confined in the bottom dot, $(\underline{1},\underline{0})$. The underlined numbers indicate the spatial locations of the electron and hole that recombine.

The presence of additional electrons or holes in the top dot introduces small energy shifts. Consequently, in the spectra we see a family of PL lines labeled $(\underline{1},\underline{n_e})$. This family of lines all have a single electron-hole pair in the bottom dot that recombine but a different number of electrons, n_e, or holes, n_h, in the top dot. Analogous families of PL lines are obtained for the intradot transitions when the bottom dot contains different numbers of charges: the positive trion $[X^+=1$ electron+2 holes, $(\underline{1},\underline{n_e})]$, negative trion $[X^-=2$ electrons+1 hole, $(\underline{2},\underline{n_e})]$, or biexciton $[XX^0=2$ electrons+2 holes, $(\underline{2},\underline{n_e})]$. The splittings between the lines of each family depend on the separation of the QDs and are not resolved in the PL spectral map for the QDM with a barrier of 16 nm. These Stark shifts of the intradot transitions allow for remote optical detection of the charge state of the other dot.[20,24] It is also worth noting that while the X^--like family is typically about 6 meV below the X^0-like family, the X^+-like family varies from about 1 meV below to about 5 meV above the X^0-like family. The shift of the XX^0 family is correlated with the variation in the X^+ family.

In both spectra in Fig. 4 we have marked the PL patterns that arise from molecular tunnel resonances in the initial and final states of the neutral, the singly charged (trion), and the doubly charged exciton transitions. While the neutral exciton exhibits just a single AC, both the singly and the doubly charged exciton show "x" patterns, which will be described in detail in Sec. IV A.[16] "x" patterns are unambiguously and self-consistently assigned to their respective charge state using features such as the magnitude of the ACs, the spin fine structure,[21] and the observation of replica ACs in the corresponding biexciton transitions.[20]

A. X patterns

The x pattern arises when there are ACs in both the initial and the final states of the optical transition and these ACs are separated in bias by only a small difference in Coulomb energy.[16] In Fig. 4 we see that both the trion and the doubly charged exciton x patterns span the energy between the trion family ($X^{\pm}$-like transitions) and the X^0-like transitions. For example, the $(\underline{1},\underline{2})$ PL line of the doubly negatively charged exciton has energy quite similar to the $(\underline{1},\underline{0})$ neutral exciton state because both states have one electron and one hole in the bottom dot. The $(\underline{2},\underline{1})$ doubly negatively charged exciton PL line has energy similar to the $(\underline{2},\underline{0})$ negative trion PL line because each has two electrons and one hole in the bottom dot. Thus the neutral excitonlike $(\underline{1},\underline{2})$ and trionlike $(\underline{2},\underline{1})$ lines define the top and bottom, respectively, of the x pattern. The negative trion x pattern spans the same range for similar reasons.

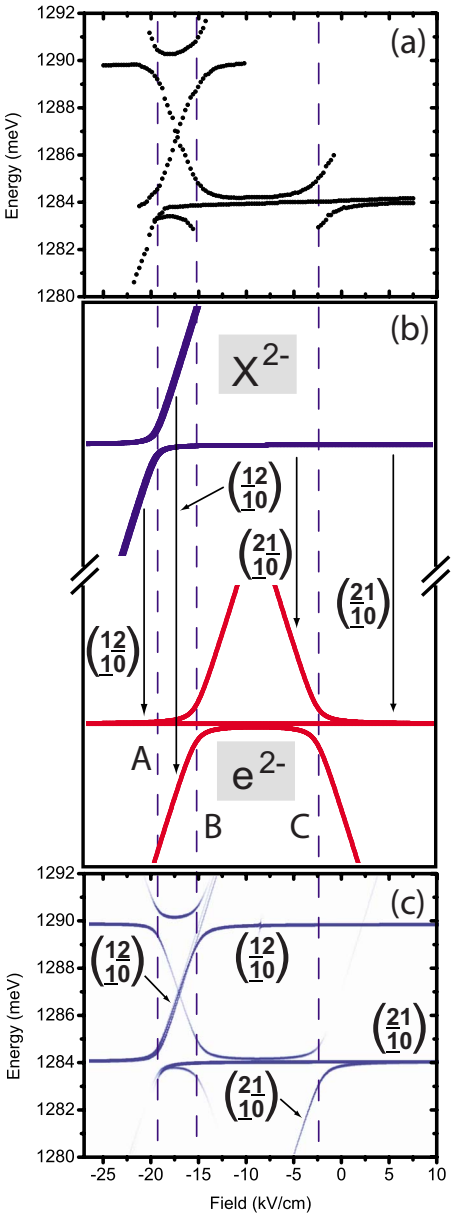

FIG. 5. (Color online) (a) Energy of experimentally observed photoluminescence lines as a function of applied electric field for a QDM with electrons tunneling through a 14 nm barrier. (b) Energies of optically excited $[X^{2-}$, blue (dark gray)] and optical ground $[e^{2-}$, red (light gray)] states calculated using values extracted from (a). (c) Calculated transition spectra using states of (b). Dashed lines A, B, and C are used to show how anticrossings in the optically excited and optical ground states appear as anticrossings in the PL spectra. Four transitions that appear in the PL spectra are indicated with vertical arrows and labeled.

In Fig. 5(a) we show the X^{2-} PL lines for a QDM where electrons tunnel through a 14 nm barrier. Because the intensity of PL lines can vary by orders of magnitude, we have extracted the energies of each PL line from a spectral map such as Fig. 4(a). On the left side of Fig. 5(a) the PL lines form the x pattern. On the right side an additional anticrossing appears. To explain the origin of these coarse features, in Fig. 5(b) we plot the energies of the optically excited (X^{2-}) and optical ground (e^{2-}) states. The calculation of these en-

ergy levels will be described in Sec. V; here only the relevant range of energy and applied electric field is displayed. In Fig. 5(c) we show a calculated transition spectrum. The energies of the calculated PL lines are determined by taking the energy difference between all possible optically excited and optical ground states. The intensities of the lines are determined by taking into account the optical selection rules and the decrease in PL intensity for the recombination of electrons and holes in different dots. More details on the calculation of energy levels and PL spectral lines are given in Sec. V D.

In Fig. 5(b) we have indicated four transitions from the optically excited (X^{2-}) to the optical ground (e^{2-}) states and labeled the corresponding PL lines in the calculated spectra [Fig. 5(c)]. The transitions $(\frac{1,2}{1,0})$ and $(\frac{2,1}{1,0})$, which are the neutral excitonlike and negative trionlike optical transitions, respectively, bound the x pattern on the top and bottom. Dashed lines A, B, and C are used to indicate how the anticrossings that appear in the PL spectra can each be attributed to a specific anticrossing in either the X^{2-} or the e^{2-} state. The x pattern in the transition spectra arises because the leftmost anticrossing of the e^{2-} state (B) occurs at a value of the applied electric field that is similar but not identical to the anticrossing in the X^{2-} state (A). The additional anticrossing at C results from a second anticrossing in the optical ground (e^{2-}) state.

Not all of the photoluminescence lines predicted by the calculation appear in the data. There are several reasons for the absence of predicted PL lines. First, higher-energy X^{2-} states can thermally relax to lower-energy states before electron-hole recombination and the emission of a photon. Consequently, some photoluminescence lines from high-energy initial states are suppressed. Second, the range of electric fields in which photoluminescence lines can be observed is limited. At large electric fields electron-hole pairs can ionize before optical recombination. At small electric fields, the optical charging of the two-electron state becomes improbable due to limited tunneling of holes to the substrate. Third, indirect photoluminescence lines can become weak due to small wave-function overlap and consequently small optical matrix elements. Despite these limitations, there is excellent agreement between the observed and calculated spectral maps in Fig. 5.

B. Doubly charged biexciton spectra

In Fig. 6 we show a spectral map for a QDM where electrons tunnel through a 14 nm barrier. The figure includes PL from the singly and doubly charged excitons along with the corresponding biexcitons. In the inset we extract the energies of each PL line and use color coding to identify the excitonic state responsible for each line. The biexciton transitions (e.g., XX^{2-}) have a replica anticrossing at the same applied electric field as one anticrossing of the corresponding excitonic x pattern (X^{2-}).[20] Similar replica anticrossings in the biexciton state appear for both the neutral (X^0,XX^0) and the singly charged exciton (X^-,XX^-).

The replica anticrossings in the XX^{2-} PL spectra arise from anticrossings in the X^{2-} state, which is both the final state of the XX^{2-} biexcitonic transition and the initial state of the X^{2-} excitonic transition. To illustrate this point, in Fig. 7 we show a complete calculated level diagram for a QDM charged with two excess electrons. The figure shows the optical ground states [e^{2-}, red (lower group)], the excitonic states [X^{2-}, blue (middle group)], and the biexcitonic states [XX^{2-}, green (upper group)]. Details on how to calculate these energy levels will be given in Sec. V. The anticrossing in the lower left of the X^{2-} state (around 1280 meV) is in the final state of the $(\frac{2,2}{2,0})$ biexcitonic transition and the initial state of the $(\frac{1,2}{1,0})$ excitonic transition.

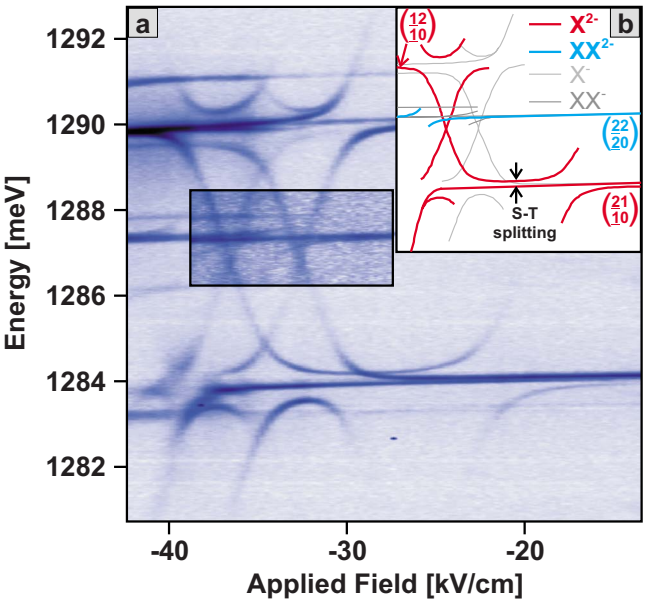

FIG. 6. (Color online) Molecular resonances in the PL transition of a QDM when it is charged with a single electron and with two electrons. Inset: Extracted transition energies for the doubly negative exciton [red (thick, gray)], the doubly negative biexciton [cyan (thick, darkest gray)], the negative trion (thin, lightest gray), and the negative biexciton (thin, dark gray). The shaded box is plotted with a different intensity scale to reveal the biexcitonic features.

C. Hole tunneling

As seen in Fig. 4, doubly positively charged QDMs also exhibit x patterns. In Fig. 8 we show the experimentally measured and calculated x patterns for a doubly positively charged QDM with holes tunneling through a 6 nm barrier. A close look at the upper left corner of the x patterns shows a fine-structure doublet, which is more clearly resolved for the case of hole tunneling than for electron tunneling. This fine structure results from spin interactions. In Sec. V we will present the state Hamiltonians, including spin interactions, and discuss why some spin fine structure is more evident for the case of hole tunneling.

V. INCLUDING COULOMB AND SPIN INTERACTIONS IN THE HAMILTONIANS

In this section we present the Hamiltonians that describe the e^{2-} and X^{2-} states, including Coulomb and spin interac-

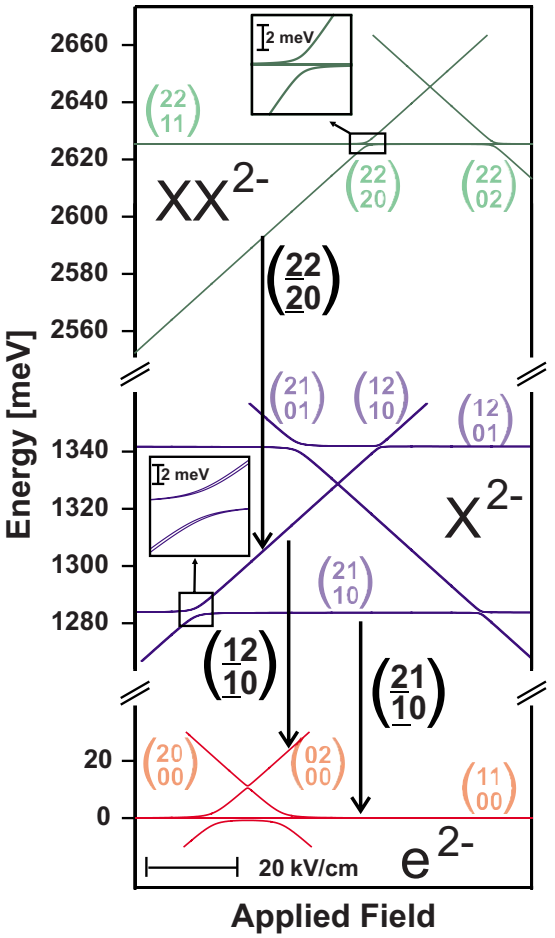

FIG. 7. (Color online) Calculated ground (red, lowest group), first optically excited (blue, middle group), and second optically excited (green, highest group) energy levels of a doubly negatively charged QDM. One XX^{2-} and two X^{2-} intradot transitions that are commonly observed in the experiments are also indicated with vertical arrows. As described in the text, energies are referenced to the $\binom{1,1}{0,0}$ configuration.

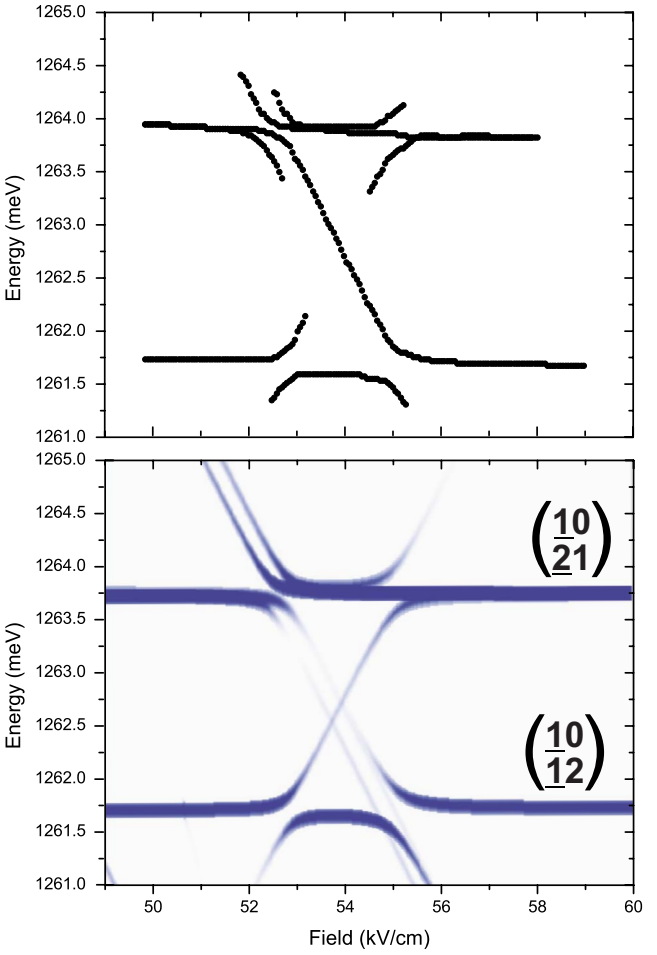

FIG. 8. (Color online) (a) Energy of experimentally observed photoluminescence lines as a function of applied electric field for a QDM with holes tunneling through a 6 nm barrier. (b) Calculated spectra using values extracted from (a). Two transitions are labeled and can be compared to Fig. 4(b) to identify the position of this x pattern relative to other charge states.

tions, at zero magnetic field. The Hamiltonians for QDMs containing two excess holes are qualitatively identical and are listed explicitly in Sec. VI. The importance of Coulomb interactions can be seen in Fig. 7. Because of the exciton binding energy, large changes in energy are determined by the total number of electron-hole pairs (e.g., e^{2-} is about 1280 meV lower than X^{2-}, which is about 1280 meV lower than XX^{2-}). For states with the same total number of charges (for example, X^{2-}), the different spatial distributions of charges [e.g., $\binom{12}{01}$ and $\binom{21}{10}$] have slightly different Coulomb interactions and thus slightly different energies. The Coulomb interactions are described by terms with the form V_{cd}^{ab}, which is the energy from the interaction between particles a and b located in dots c and d. Because the two dots are not identical, the Coulomb energy between two particles confined in the bottom dot (for example, two electrons: V_{BB}^{ee}) differs slightly from the Coulomb energy between two particles confined in the top dot (V_{TT}^{ee}) or in separate dots (V_{BT}^{ee}). The Coulomb energy terms are discussed in detail in the Appendix.

To include spin interactions, we must consider not just the spatial distribution of charges but also the spin orientation of each charge. We will continue to use the $\binom{m_e,n_e}{m_h,n_h}$ notation, but we will now explicitly list the spin orientation for each charge. We will use $\uparrow,\downarrow$ and $\Uparrow,\Downarrow$ to denote the spin orientations of electrons and holes. The hole spin is really a spinor orientation, although it is dominated by the $\pm 3/2$ heavy-hole contribution to the spinor.[44] When there are two electrons or two holes present, we will add an additional subscript (S or T) to differentiate between singlet and triplet configurations. So, for example, $\binom{\downarrow,\uparrow}{0,0}_S$ indicates a QDM with one electron in each of the dots where the two spins are collectively in a singlet state [i.e., $\binom{\downarrow,\uparrow}{0,0}_S = \frac{1}{\sqrt{2}}(\downarrow,\uparrow - \uparrow,\downarrow)$].

We continue to use the atomiclike states where electrons and holes are localized in individual dots as the basis states for Hamiltonians that describe the tunnel coupling, Coulomb, and spin interactions. We focus our discussion of each Hamiltonian on the spin interactions unique to that total charge state. Because tunneling is a spin-conserving process, only states with the same total spin projection are coupled

together. Molecular states are thus superpositions of different atomiclike states with the same total spin projection.

For electron tunneling in a *p*-type Schottky diode, the applied electric field creates a substantial energy difference between the confined hole energy levels. As a result, all observed PL lines originate in states where the holes are in the bottom QD. For the sake of clarity, we include only the states with the holes in the bottom dot in the Hamiltonians presented here. Note that the energy levels in Fig. 7 are calculated using all possible spin and charge distributions. Energies are referenced to $\binom{1,1}{0,0}$, the state with one electron in each dot. $\binom{1,1}{0,0}$ therefore has zero energy and no dependence of energy on the applied electric field. States that have an unequal net charge in the two dots have an energy that depends on the applied electric field and therefore a large Stark shift.

A. e^{2-} state: Kinetic exchange

We consider first the optical ground (e^{2-}) state, which contains only two electrons. There are three possible spatial distributions: (1) both electrons in the bottom dot, (2) one electron in each dot, and (3) both electrons in the top dot. When both electrons are in the same dot, the Pauli principle requires them to be in a spin singlet. When the electrons are located in separate dots, singlet and triplet configurations of the spins are possible. There are thus six possible spin configurations and the system can be described by a Hamiltonian of the following form:

$$\hat{H}^{e^{2-}} = \begin{array}{c} \begin{matrix} \binom{\downarrow\uparrow,0}{0,0}_S & \binom{\downarrow,\uparrow}{0,0}_S & \binom{\downarrow,\uparrow}{0,0}_T & \binom{\downarrow,\downarrow}{0,0}_T & \binom{\uparrow,\uparrow}{0,0}_T & \binom{0,\downarrow\uparrow}{0,0}_S \end{matrix} \\ \begin{pmatrix} V_{BB}^{ee} - edF & -\sqrt{2}t & 0 & 0 & 0 & 0 \\ -\sqrt{2}t & V_{BT}^{ee} & 0 & 0 & 0 & -\sqrt{2}t \\ 0 & 0 & V_{BT}^{ee} & 0 & 0 & 0 \\ 0 & 0 & 0 & V_{BT}^{ee} & 0 & 0 \\ 0 & 0 & 0 & 0 & V_{BT}^{ee} & 0 \\ 0 & -\sqrt{2}t & 0 & 0 & 0 & V_{TT}^{ee} + edF \end{pmatrix} \end{array}. \tag{2}$$

The additional factor of $\sqrt{2}$ for the tunneling rate arises because either electron can tunnel.[45]

Because tunneling is spin preserving, only the $\binom{\downarrow,\uparrow}{0,0}_S$ state can couple to the $\binom{\downarrow\uparrow,0}{0,0}_S$ and $\binom{0,\downarrow\uparrow}{0,0}_S$ states. In the Hamiltonian matrix this is expressed by the nonzero off-diagonal matrix elements with a value of $-\sqrt{2}t$, which create anticrossings and molecular orbitals that are superpositions of the singlet states. The triplet configurations cannot tunnel couple and consequently do not anticross. The tunnel coupling of singlets but not that of triplets induces a splitting between the singlet and the triplet states at anticrossings. Because of its origin in tunneling, this energy splitting between singlet and triplet states is called kinetic exchange.[41]

The kinetic exchange interaction is somewhat different from the usual exchange Coulomb interaction. First, the singlet line has both upper and lower branches with different molecular-orbital characters. Second, the degree of separation between singlet and triplet states depends on the applied electric field, as shown in the inset of Fig. 9. Moreover, the separation between singlet and triplet states is influenced by the kinetic exchange at two separate anticrossing points. See, for example, the ACs labeled B and C in Fig. 5 and the inset of Fig. 9.

Each of the two anticrossings (e.g., B and C in Fig. 5) occur when the state that has one electron in each dot becomes resonant with a state that has two electrons in the same dot. Because of slight asymmetry between the dots, these resonances happen at slightly different values of the applied electric field. The energy difference between the two anticrossing points is given by differences in the Coulomb interaction energy: $U=(V_{BB}^{ee}+V_{TT}^{ee}-2V_{BT}^{ee})/2$. This energy difference results in an electric-field separation between the two tunnel resonances of $2U/ed$.

Away from resonance, the singlet and triplet states return to energy degeneracy. If the tunneling rate $\sqrt{2}t$ becomes comparable to U, the singlet and triplet states are unable to return to degeneracy between the two primary tunnel resonances. The singlet and triplet then remain split between the two anticrossing points as shown in the inset of Fig. 9. The lines are separated by a "singlet-triplet (S-T) splitting" with the singlet at lower energy than the triplet. This singlet-triplet splitting can also be seen clearly in Figs. 6 and 5(a). In the data, the PL line resulting from optical recombination to the singlet state is at higher energy than the PL line from optical recombination to the triplet state. The energy order of the singlet and triplet appears in reverse because the two-electron states shown in the inset of Fig. 9 are the *final* states of the optical transitions responsible for the PL lines in Figs. 6 and 5(a). A transition that ends in the lowest-energy state (singlet) therefore has greater PL energy.

Halfway between the two tunnel resonances the singlet-triplet splitting is given by

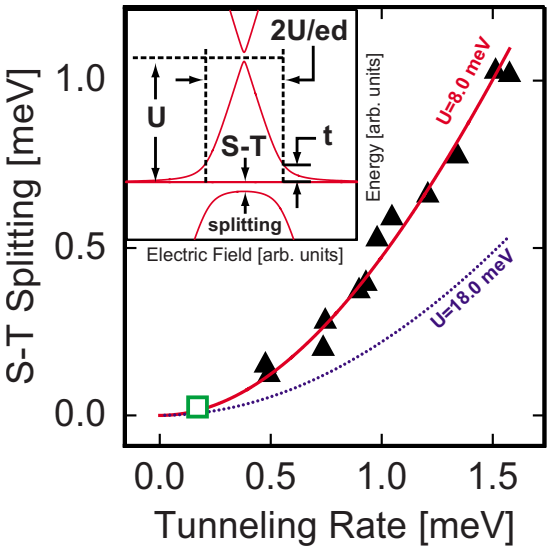

FIG. 9. (Color online) Absolute value of the singlet-triplet (S-T) splitting as a function of the tunneling rate t as defined in the inset. The solid line is a fit to the data according to Eq. (3) with $U=8.0$ meV. The green open square is the value of the S-T splitting measured on a doubly positively charged QDM with 6 nm barrier and hole tunneling. The blue dashed curve is calculated with $U=18$ meV, which corresponds to the case of hole tunneling. Inset: Energy levels of two electrons (holes) in a QDM.

$$\Delta_{\text{S-T}} = \frac{1}{2}(\sqrt{U^2 + 8t^2} - U). \tag{3}$$

A fit to the measured singlet-triplet splitting of several QDMs ($10\ \text{nm} \geq d \leq 16\ \text{nm}$) as a function of the tunneling rate yields $U=8.0$ meV. This agrees well with the independently measured separation of the two ACs.[46] For the case of two holes we find that $U=18$ meV, which also is plotted in Fig. 9.

B. X^{2-} state: Electron-hole exchange

The X^{2-} state contains three electrons and one hole. Since there cannot be more than two electrons occupying any state, there are only two spatial distributions of electrons: (1) two electrons in the bottom dot with one electron in the top dot or (2) one electron in the bottom dot and two electrons in the top dot. Likewise, there are two spatial configurations for the additional hole—either in the bottom or in the top QD. Consequently, there are 4 possible spatial configurations and 16 possible spin configurations.[47]

We need to consider only four of these spin configurations to explain the electron-hole exchange interactions, so we restrict the following discussion to the case of electron tunneling with the hole confined to the bottom dot with spin up. The four spin configurations are $\binom{\uparrow\downarrow,\uparrow}{\Uparrow,0}$, $\binom{\uparrow\downarrow,\downarrow}{\Uparrow,0}$, $\binom{\uparrow,\uparrow\downarrow}{\Uparrow,0}$, and $\binom{\downarrow,\uparrow\downarrow}{\Uparrow,0}$. Note that the spin structure of X^{2-} is equivalent to that of X^0 because there is only one unpaired electron and hole. The two spin-paired electrons play no role in the spin interactions.

The Hamiltonian that corresponds to these four basis states fully captures the physics of electron-hole exchange in the vicinity of a QD molecular tunnel resonance. The Hamiltonian for the case with hole spin down can be determined by inverting the orientation of all spins in each basis state,

$$\hat{H}_X^{2-} = E_0\hat{I} + \begin{pmatrix} \binom{\uparrow\downarrow,\uparrow}{\Uparrow,} & \binom{\uparrow\downarrow,\downarrow}{\Uparrow,0} & \binom{\uparrow,\uparrow\downarrow}{\Uparrow,0} & \binom{\downarrow,\uparrow\downarrow}{\Uparrow,0} \\ \Gamma & 0 & t & 0 \\ 0 & \Gamma & 0 & t \\ t & 0 & edF - J_{\text{e-h}} & 0 \\ 0 & t & 0 & edF + J_{\text{e-h}} \end{pmatrix}. \tag{4}$$

E_0 is the exciton energy and $\hat{I}$ is the identity matrix. The basis states always have two electrons in one dot and one electron in the second dot. The Pauli principle requires that the pair of electrons in a single dot must be in a spin singlet. Because tunneling is a spin-conserving process, only a single electron can tunnel between the dots. For example, if there are two spin-up and one spin-down electrons, the two spin-up electrons must be in separate dots and only the spin-down electron can tunnel. In contrast, in the e^{2-} state either of the two electrons can tunnel through the barrier, which results in the additional factor of $\sqrt{2}$ for the tunneling matrix element in Eq. (2). Γ captures the energy shift between the two spatial distributions of electrons, which results from different Coulomb interactions with the hole and the asymmetry between the two dots. The definition of Γ as sums of and differences between the Coulomb terms V_{cd}^{ab} is provided in the Appendix. Γ determines the values of the applied electric field where states become degenerate in energy. $J_{\text{e-h}}$ is the (isotropic) electron-hole exchange interaction. Here we chose $J_{\text{e-h}} \neq 0$ only for the configurations where a single electron and single hole are in the same dot. This is consistent with experimental observations within the limits of our current experimental resolution. We note that we have ignored the presence of aniostropic electron-hole (e-h) exchange, which will cause splittings in the X^{2-} and X^{2+} but which is below the resolution of our PL measurements.

In the top part of Fig. 10(a) we plot the eigenenergies of the X^{2-} in the vicinity of the electron-tunneling resonance. As the states pass through the molecular resonance, the $\binom{1,2}{1,0}$ states, where electron-hole exchange is active, evolve into the $\binom{2,1}{1,0}$ states, where electron-hole exchange is strongly suppressed. Consequently, the splitting induced by the electron-hole exchange is gradually reduced. Far away from the resonance the splitting induced by electron-hole exchange is $2J_{\text{e-h}}$; in the center of the AC the splitting is reduced to $J_{\text{e-h}}$.

The fine-structure splitting induced by electron-hole exchange should be mapped by the PL spectrum, but in the measured spectrum in Fig. 6 or 5 it is not observed. There are two primary reasons for the absence of the splitting induced by electron-hole exchange in the X^{2-} PL spectrum. For our explanation we focus on the center of the X^{2-}-tunneling resonance, where the interdot transitions $\binom{1,2}{\downarrow,0}$, which contain the information of the electron-hole exchange splitting, are optically strong and where the splitting has dropped to only half its value.

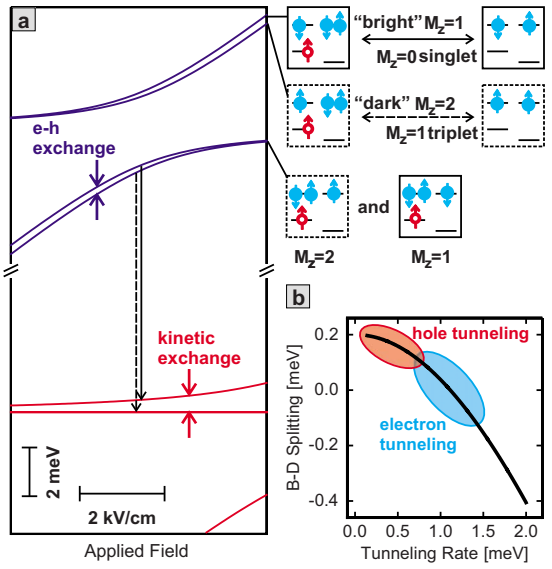

FIG. 10. (Color online) (a) Energy levels of the doubly negative exciton (blue, top group) and the two electrons (red, bottom group) in the vicinity of the electron-tunneling resonance where the hole is in the bottom QD. The cartoons on the right give the spin configurations for the different states. Tunneling and optical selection rules couple only the configurations in the dashed (solid) boxes. (b) Splitting between the $M_z=1\rightarrow M_z=0$ transition (bright singlet) and the $M_z=2\rightarrow M_z=1$ transition (dark triplet) as a function of tunneling rate in the final state according to Eq. (5) with $J_{\text{e-h}}=0.2$ meV and $\Gamma=6$ meV. The shaded areas indicate roughly the expected splitting for the typically achieved tunneling rates for QDMs with hole (red, upper highlight) and electron (blue, lower highlight) tunneling. Note: The calculation in panel (a) is valid for any dot separation.

The first reason for the absence of the electron-hole exchange induced splitting in the PL splitting is a competition between electron-hole and kinetic exchange. The center of the X^{2-} AC is always close in electric field (about 6 meV/ed) to the corresponding two-electron AC in the final state of the optical transition. See, for example, the proximity between lines A and B in Fig. 5. When the electron-tunneling rate is sufficiently large, a residual kinetic exchange splitting still exists in the final state even at the applied electric field at the center of the X^{2-} AC. Figure 10(a) provides a detailed look at this residual splitting. Because the two states split by the electron-hole exchange interaction recombine to different final states (one to the singlet and one to the triplet), the splitting of the PL lines is determined by a competition between the electron-hole exchange splitting in the initial X^{2-} state and the kinetic exchange splitting in the final e^{2-} state.

More specifically, the lower-energy electron-hole exchange-split state is a superposition of the $(\uparrow\downarrow,\uparrow)$ and $(\uparrow,\uparrow\downarrow)$ states coupled together by tunneling. Optically allowed recombination from this superposition ends in the $(\uparrow,\uparrow)_T$ triplet state. On the other hand, the higher-energy electron-hole exchange-split state is a superposition of $(\uparrow\downarrow,\downarrow)$ and $(\downarrow,\uparrow\downarrow)$, which recombine to the $(\uparrow,\downarrow)_S$ singlet state.[48] The total splitting of the PL lines, with contributions from both the electron-hole exchange splitting of the initial X^{2-} states and the kinetic exchange splitting of the final e^{2-} states, is given by

$$\Delta^{\text{exch}} = J_{\text{e-h}} + \frac{s}{2} - \sqrt{s^2/4 + 2t^2}, \tag{5}$$

where s measures the separation between the two ACs of the initial and final states in meV (here $s=6$ meV). The result for $J_{\text{e-h}}=0.2$ meV is plotted in Fig. 10(b). We find that the splitting of the PL lines should be around zero for the tunneling rates that we typically observe in QDMs with electron tunneling.

The second reason that fine-structure splitting induced by electron-hole exchange is difficult to resolve is that the energy of interdot transitions depends strongly on applied electric field. Consequently, small fluctuations in the local electric field at the QDM can induce large shifts in the transition energy. These fluctuations cause the interdot transition to broaden spectrally. In QDMs with large dot separation, which are typical for studies of electron tunneling, the linewidths for interdot transitions can be as large as 500 μeV. QDMs that exhibit hole tunneling typically have relatively small tunneling rates even at dot separations that are two to three times smaller than the dot separation for QDMs with electron tunneling.[17] This results in a negligible kinetic exchange splitting in the final state and in sharper interdot transitions. Consequently, a much clearer optical spectrum that resolves the spin fine structure is obtained from doubly positively charged QDMs that exhibit hole tunneling. See, for example, Fig. 8.

C. XX^{2-} state

As shown in Fig. 1(c), in the XX^{2-} state the electron energy levels of each dot are fully occupied with two electrons each. Consequently, electrons cannot tunnel between the two dots. There are, however, two holes that can be distributed between the energy levels of the two dots and couple the energy levels via coherent tunneling. The Hamiltonian for the XX^{2-} state is therefore identical to the Hamiltonian for the h^{2+} state, with the addition of minor corrections due to the change in Coulomb interactions with the electrons. The Hamiltonian for the h^{2+} state is presented explicitly in Sec. VI, so we do not repeat it here. The h^{2+} state Hamiltonian is analogous to the Hamiltonian for the e^{2-} state at zero magnetic field. The only change is the reduced magnitude of the tunneling matrix element due to the heavier hole effective mass, which reduces the magnitude of the anticrossings. This can be seen clearly in Fig. 7, where the XX^{2-} and e^{2-} states have qualitatively identical energy levels. The only quantitative differences are the position of the anticrossings, which are determined by the Coulomb offsets, and the magnitudes of the anticrossings.

D. Calculational parameters

The Hamiltonians presented above require input values of the parameters, which can be extracted directly from the measured spectra. For example, in Fig. 5(a) the two horizontal lines at 1284 and 1290 meV arise from "direct" recombi-

TABLE I. Parameters extracted from experimental spectral maps and used to generate calculated spectral maps. Values are in meV except d, which is in meV/V.

	6 nm hole	2 nm hole	14 nm electron
E_0	1261	1294	1290
Γ	2.17	1.2	−5.71
Ω	8	10.85	17.12
d	24.41	10.58	35.67
t	0.1462	0.86	0.566
$J_{\text{e-h}}$	0.1725	0.1553	0.200

nation of an electron and hole both located in the bottom dot. The energy difference between these lines is caused by the spectator electrons. When both spectator electrons are in the top dot, the PL line has an energy similar to that of the neutral exciton family of PL lines. When one of the spectator electrons is in the bottom dot, the energy shifts by 6 meV, characteristic of the negative trion family of lines. From this shift we determine Γ, the difference in Coulomb energies between these two configurations. The slope of the diagonal lines in Fig. 5(a) determines d, which we generally find to be in reasonable agreement with the slope predicted using the thickness of the barrier. The combination of Γ and d determines the change in applied electric field required to move between the two anticrossing points (A and B in Fig. 5). Anticrossings at A in Fig. 5(a) arise from the anticrossing of the X^{2-} state. From this anticrossing we measure t. Anticrossings at B and C in Fig. 5(a) arise from the e^{2-} state; from this anticrossing gap we confirm the magnitude of $\sqrt{2}t$.

The energies of the X^{2-} and e^{2-} states shown in Fig. 5(b) are calculated using Eqs. (2) and (4) and the parameter values extracted from the data. For comparison with the observed spectral map in Fig. 5(a), we take the difference between the initial- and the final-state energies and factor in the strength of the optical transitions to generate the calculated spectral map shown in Fig. 5(c). Such calculated spectral maps are a fit to the data in the sense that the values of individual parameters used in the calculation are extracted directly from the data as described above. Individual parameters are varied to achieve a best fit only when incomplete spectral maps prevent direct extraction of the actual value from the data. The specific values extracted from the data and used in the calculations can be found in Table. I. The excellent agreement between the observed and calculated spectra confirms that the matrix descriptions of the states in Eqs. (2) and (4) capture the essential physics, including spin interactions, of these states.

As a final validation of the matrix Hamiltonians presented here, in Fig. 11 we show the experimentally observed and calculated spectral maps for a sample with holes tunneling through a 2 nm barrier. There appears to be a qualitative difference between Figs. 11 and 8, but this difference is entirely explained by the thinner barrier. The thinner barrier leads to substantially larger tunneling rates and therefore results in singlet and triplet states that remain separated throughout the observed range of applied electric field, as discussed in Sec. V A. This effect is reproduced in the calculated spectra that use the larger tunneling parameter. Not all of the lines predicted by the calculated spectral map appear in the data because the thin barrier enables rapid thermal relaxation of high-energy initial states before emission of a photon.

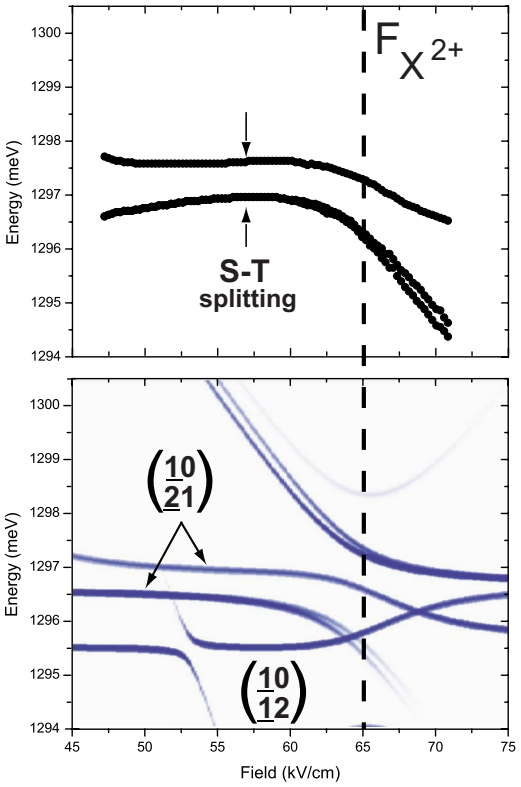

FIG. 11. (Color online) (a) Energy of experimentally observed photoluminescence lines as a function of applied electric field for a QDM with holes tunneling through a 2 nm barrier. The S-T splitting is indicated. (b) Calculated spectra using values extracted from (a). Two transitions are labeled; $\binom{1,0}{2,1}$ points to two lines because the transition can end in the singlet (upper PL line) or triplet (lower PL line) configuration of $\binom{0,0}{1,1}$. $F_{X^{2+}}$ indicates the electric field at which the anticrossings of the X^{2+} states occur.

VI. APPLIED MAGNETIC FIELDS

Application of a magnetic field lifts the degeneracy between opposing spin projections and leads to a Zeeman splitting that is proportional to both the applied magnetic field and the g factor. Because the g factor depends on material parameters, it depends on the amplitude of the wave function in regions with different material compositions and can thus be used to identify the orbital character of molecular states.[22] We apply a magnetic field along the optical axis of the emitted photoluminescence (Faraday geometry) by placing the sample in the bore of a split coil superconducting magnet and positioning the sample under the focus of a 0.45 numerical aperture (NA) lens using low-temperature nonmagnetic translation stages.

Our discussion of magnetic fields will focus on the states of a doubly positively charged QDM (h^{2+} and X^{2+}) where holes tunnel between the dots. We will first discuss the Zee-

man splitting, which depends on the spin orientations of any unpaired electrons and holes. We will then consider how the formation of molecular orbitals changes the amplitude of hole wave functions and leads to resonant changes in the g factor and thus in the Zeeman splitting.

A. Zeeman splitting

To include magnetic fields, we must add a Zeeman term to the Hamiltonians. We will consider only QDMs with a thin tunnel barrier where t remains positive.[23] If we restrict ourselves to magnetic fields in the Faraday geometry, the Zeeman interaction term has the form[49]

$$\hat{H}_{\text{Zeeman}}(B) = \mu_B\left(g_e S_e - \frac{g_h}{3}\hat{J}_h\right)B, \tag{6}$$

with μ_B as the Bohr magneton, g_e as the longitudinal electron g factor, g_h as the longitudinal heavy-hole g factor, S_e as the electron-spin projection $(\pm 1/2)$, J_h as the heavy-hole spin projection $(\pm 3/2)$, and B as the magnetic field. For easy comparison, we will present the basis states as well as the zero magnetic field and Zeeman terms of the Hamiltonians.

The Hamiltonian for the optical ground state (h^{2+}) is

$$\hat{H}^{h^{2+}} = \begin{array}{c} \begin{matrix} \begin{pmatrix} 0,0 \\ \Downarrow\Uparrow,0 \end{pmatrix}_S & \begin{pmatrix} 0,0 \\ \Downarrow,\Uparrow \end{pmatrix}_S & \begin{pmatrix} 0,0 \\ \Downarrow,\Uparrow \end{pmatrix}_T & \begin{pmatrix} 0,0 \\ \Downarrow,\Downarrow \end{pmatrix}_T & \begin{pmatrix} 0,0 \\ \Uparrow,\Uparrow \end{pmatrix}_T & \begin{pmatrix} 0,0 \\ 0,\Downarrow\Uparrow \end{pmatrix}_S \end{matrix} \\ \begin{pmatrix} \Gamma_2 - edF & -\sqrt{2}t & 0 & 0 & 0 & 0 \\ -\sqrt{2}t & 0 & 0 & 0 & 0 & -\sqrt{2}t \\ 0 & 0 & 0 & 0 & 0 & 0 \\ 0 & 0 & 0 & 2\eta g_h & 0 & 0 \\ 0 & 0 & 0 & 0 & -2\eta g_h & 0 \\ 0 & -\sqrt{2}t & 0 & 0 & 0 & \Gamma_3 + edF \end{pmatrix} \end{array}, \tag{7}$$

where Γ_2 and Γ_3 are energy shifts due to the Coulomb interactions (V_{cd}^{ab}) whose explicit definition is given in the Appendix and $\eta = \frac{\mu_B B}{2}$. The addition of magnetic fields is quite simple in this case because the net g factor for a pair of oppositely oriented spins is zero. Only two states have any unpaired holes; in each case the net g factor for the two parallel spins is simply twice the single spin g factor. The spin orientation determines the sign of the contribution from the g factor: a hole with spin up corresponds to $-g_h$ because of the minus sign for holes in Eq. (6).

The Hamiltonian for the optically excited state (X^{2+}) is

$$\hat{H}^{X^{2+}} = \begin{array}{c} \begin{matrix} \begin{pmatrix} \uparrow,0 \\ \Downarrow\Uparrow,\Downarrow \end{pmatrix} & \begin{pmatrix} \downarrow,0 \\ \Downarrow\Uparrow,\Uparrow \end{pmatrix} & \begin{pmatrix} \uparrow,0 \\ \Downarrow\Uparrow,\Uparrow \end{pmatrix} & \begin{pmatrix} \downarrow,0 \\ \Downarrow\Uparrow,\Downarrow \end{pmatrix} & \begin{pmatrix} \uparrow,0 \\ \Downarrow,\Downarrow\Uparrow \end{pmatrix} & \begin{pmatrix} \downarrow,0 \\ \Uparrow,\Downarrow\Uparrow \end{pmatrix} & \begin{pmatrix} \uparrow,0 \\ \Uparrow,\Downarrow\Uparrow \end{pmatrix} & \begin{pmatrix} \downarrow,0 \\ \Downarrow,\Downarrow\Uparrow \end{pmatrix} \end{matrix} \\ \begin{pmatrix} \Gamma_4 + \eta(g_e+g_h) & 0 & 0 & 0 & t+\eta g' & 0 & 0 & 0 \\ 0 & \Gamma_4 - \eta(g_e+g_h) & 0 & 0 & 0 & t-\eta g' & 0 & 0 \\ 0 & 0 & \Gamma_4 + \eta(g_e-g_h) & 0 & 0 & 0 & t-\eta g' & 0 \\ 0 & 0 & 0 & \Gamma_4 - \eta(g_e-g_h) & 0 & 0 & 0 & t+\eta g' \\ t+\eta g' & 0 & 0 & 0 & \Upsilon^+ + \eta(g_e+g_h) & 0 & 0 & 0 \\ 0 & t-\eta g' & 0 & 0 & 0 & \Upsilon^+ - \eta(g_e+g_h) & 0 & 0 \\ 0 & 0 & t-\eta g' & 0 & 0 & 0 & \Upsilon^- + \eta(g_e-g_h) & 0 \\ 0 & 0 & 0 & t+\eta g' & 0 & 0 & 0 & \Upsilon^- - \eta(g_e-g_h) \end{pmatrix} \end{array}, \tag{8}$$

where Γ_4 is again an energy shift resulting from Coulomb interactions explicitly defined in the Appendix and $\Upsilon^{+(-)} = edF \pm J^{\text{e-h}}$. g' is the contribution to the g factor from the amplitude of the wave function in the barrier, which will be discussed in detail in Sec. VI B.

To illustrate the contribution of the Zeeman splitting terms, in Figs. 12(a) and 12(b) we set $g'=0$ and calculate the energies of the X^{2+} and h^{2+} states as a function of increasing magnetic field. The parameters used in the calculation are those extracted from Fig. 11 for a QDM with 2 nm barrier and given in Table I. The calculations are performed for a fixed value of applied electric field; for clarity only a subset of all lines is shown. The values of the electron and hole g factors used in the calculation are extracted from magneto-

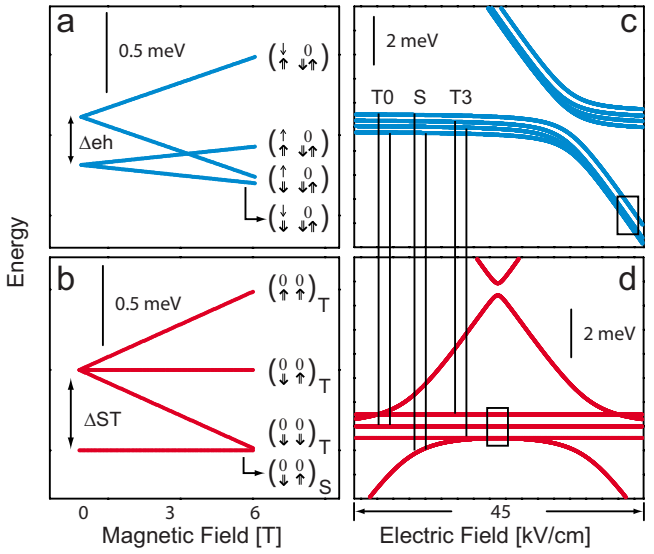

FIG. 12. (Color online) Zeeman splitting of (a) X^{2+} and (b) h^{2+} states calculated at a fixed value of the applied electric field. Calculated energies of the (c) X^{2+} and (d) h^{2+} states as a function of applied electric field for a fixed magnetic field of $B=6$ T. The boxes indicate the electric field at which the Zeeman splittings in panels (a) and (b) were calculated. Optically allowed singlet (S) and triplet (T0 and T3) transitions are indicated.

photoluminescence spectra taken on this specific molecule. The independent values for electron and hole g factors are obtained by analysis of spectra taken at several angles of the magnetic field (not shown).[50] The values obtained are $g_e=-0.745$ and $g_h=-1.4$.

The X^{2+} states have Zeeman splittings that parallel the neutral exciton. In analogy with the bright exciton, $\left(\begin{smallmatrix}\uparrow,0\\ \Downarrow,\Uparrow\end{smallmatrix}\right)$ and $\left(\begin{smallmatrix}\downarrow,0\\ \Uparrow,\Downarrow\end{smallmatrix}\right)$ have a net g factor that is the sum of the electron and hole g factors. Similarly, in analogy with the dark neutral exciton, $\left(\begin{smallmatrix}\uparrow,0\\ \Uparrow,\Uparrow\end{smallmatrix}\right)$ and $\left(\begin{smallmatrix}\downarrow,0\\ \Downarrow,\Downarrow\end{smallmatrix}\right)$ have a net g factor that is the difference between the electron and hole g factors. The small value of this difference results in the smaller Zeeman splitting between these lines. Unlike the dark neutral exciton, these states are optically active because holes of either spin projection are available in the bottom dot for recombination with the electron. The h^{2+} states contain no electrons, so their Zeeman splitting is determined entirely by the orientation of the two holes. Because they have a pair of oppositely oriented spins, the singlet and triplet with total angular momentum zero do not split. The triplets with total angular momentum 3, which have two holes with parallel spin, split by twice the hole g factor.

The energy order of the lines shown in Figs. 12(a) and 12(b) depends on the magnitude of the electron-hole exchange splitting ($\Delta_{e\text{-}h}$) and singlet-triplet splitting ($\Delta_{S\text{-}T}$). As discussed in Sec. V, these splittings are a function of the applied electric field. In Figs. 12(c) and 12(d) we plot the calculated energies of the X^{2+} and h^{2+} states as a function of applied electric field for a fixed magnetic field of 6 T. The resonant contribution of the barrier is neglected in Fig. 12.

The Zeeman splitting of optically active photoluminescence lines is given by the difference between the Zeeman splittings in the X^{2+} and h^{2+} states. Since the optical selection rules require that recombining electrons and holes have opposite spin orientations, the net g factor for an optically allowed transition is always given by the sum of the electron and hole g factors. To see how this occurs, we consider the net Zeeman splitting for the three optical transitions labeled in Figs. 12(c) and 12(d), which end in singlet and triplet optical ground (h^{2+}) states. Because of the tunnel coupling, the initial states before emission of a photon are superpositions of X^{2+} states with the same spin projection. The parameters α and β give the relative weights of the two components of this superposition. The magnitudes of α and β (not shown) depend on the applied electric field. The constant factor $\mu_B B/2$ has been suppressed,

$$\begin{aligned}
&\alpha\left(\begin{smallmatrix}\uparrow,0\\ \Downarrow,\Downarrow\Uparrow\end{smallmatrix}\right)+\beta\left(\begin{smallmatrix}\uparrow,0\\ \Downarrow\Uparrow,\Downarrow\end{smallmatrix}\right) \rightarrow \left(\begin{smallmatrix}0,0\\ \Downarrow,\Uparrow\end{smallmatrix}\right)_S \\
&(g_e+g_h) \quad - \quad 0 \quad = \quad (g_e+g_h),\\
&\alpha\left(\begin{smallmatrix}\downarrow,0\\ \Uparrow,\Downarrow\Uparrow\end{smallmatrix}\right)+\beta\left(\begin{smallmatrix}\downarrow,0\\ \Downarrow\Uparrow,\Uparrow\end{smallmatrix}\right) \rightarrow \left(\begin{smallmatrix}0,0\\ \Downarrow,\Uparrow\end{smallmatrix}\right)_S \\
&-(g_e+g_h) \quad - \quad 0 \quad = \quad -(g_e+g_h),\\
&\alpha\left(\begin{smallmatrix}\uparrow,0\\ \Downarrow,\Downarrow\Uparrow\end{smallmatrix}\right)+\beta\left(\begin{smallmatrix}\uparrow,0\\ \Downarrow\Uparrow,\Downarrow\end{smallmatrix}\right) \rightarrow \left(\begin{smallmatrix}0,0\\ \Downarrow,\Uparrow\end{smallmatrix}\right)_T \\
&(g_e+g_h) \quad - \quad 0 \quad = \quad (g_e+g_h),\\
&\alpha\left(\begin{smallmatrix}\downarrow,0\\ \Uparrow,\Downarrow\Uparrow\end{smallmatrix}\right)+\beta\left(\begin{smallmatrix}\downarrow,0\\ \Downarrow\Uparrow,\Uparrow\end{smallmatrix}\right) \rightarrow \left(\begin{smallmatrix}0,0\\ \Downarrow,\Uparrow\end{smallmatrix}\right)_T \\
&-(g_e+g_h) \quad - \quad 0 \quad = \quad -(g_e+g_h)\\
&\alpha\left(\begin{smallmatrix}\uparrow,0\\ \Uparrow,\Downarrow\Uparrow\end{smallmatrix}\right)+\beta\left(\begin{smallmatrix}\uparrow,0\\ \Downarrow\Uparrow,\Uparrow\end{smallmatrix}\right) \rightarrow \left(\begin{smallmatrix}0,0\\ \Uparrow,\Uparrow\end{smallmatrix}\right)_T \\
&(g_e-g_h) \quad - \quad (-2g_h) \quad = \quad (g_e+g_h),\\
&\alpha\left(\begin{smallmatrix}\downarrow,0\\ \Downarrow,\Downarrow\Uparrow\end{smallmatrix}\right)+\beta\left(\begin{smallmatrix}\downarrow,0\\ \Downarrow\Uparrow,\Downarrow\end{smallmatrix}\right) \rightarrow \left(\begin{smallmatrix}0,0\\ \Downarrow,\Downarrow\end{smallmatrix}\right)_T \\
&(-g_e+g_h) \quad - \quad 2g_h \quad = \quad -(g_e+g_h).
\end{aligned} \tag{9}$$

A schematic level diagram for these transitions is presented in Fig. 13. The diagrams for optical recombination to the $\left(\begin{smallmatrix}0,0\\ \Downarrow,\Uparrow\end{smallmatrix}\right)_S$ singlet state are identical to the $\left(\begin{smallmatrix}0,0\\ \Downarrow,\Uparrow\end{smallmatrix}\right)_T$ triplet case ($m=0$). The optical selection rules lead to the prediction that the application of magnetic fields will result in a doubling of the spectral map observed at zero field. The two copies should be separated by a constant Zeeman splitting given simply by the total g factor (g_e+g_h) as depicted in the middle panels of Fig. 13 ("$B>0$ off-resonance"). In the right panels of Fig. 13 we add the resonant contribution of the barrier, which is known to create electric-field-dependent g factors.[22]

B. Resonant changes in g factor

Because the g factor depends on material parameters, it is sensitive to the amplitude of the wave function in regions

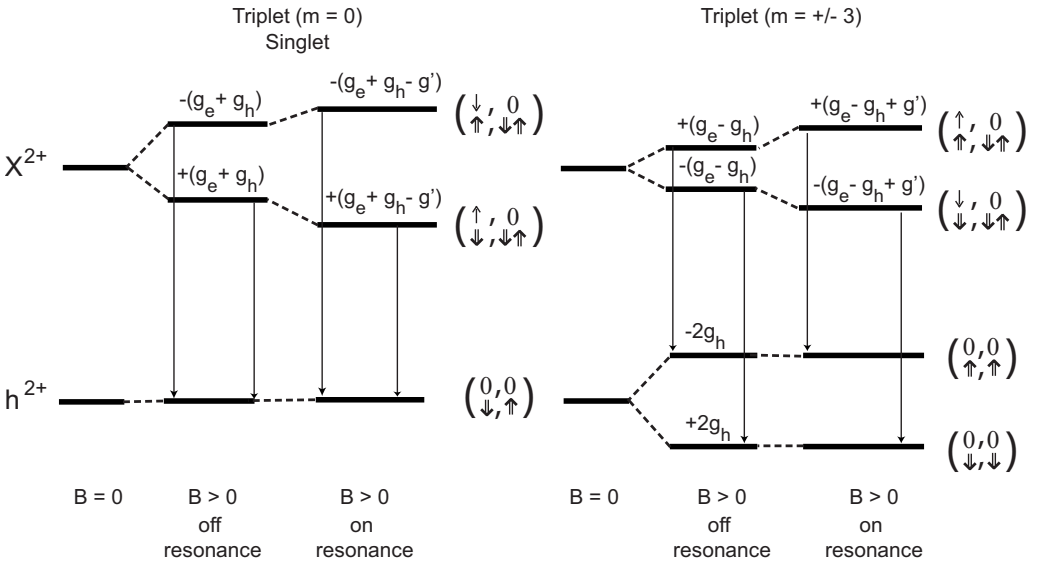

FIG. 13. Schematic depiction of the Zeeman splitting for optical transitions ending in the singlet and $m=0$ and $m=\pm 1$ triplet states. The resonant changes in splitting are specific to X^{2+} states in the low-energy molecular branch, which displays antibonding character.

comprised of different materials.[51,52] In the particular case of our QDMs, the g factor for holes in InAs dots is negative, while the g factor for holes in bulk GaAs is positive.[53] Resonant changes in the amplitude of the wave function in the GaAs barrier arise at anticrossings due to the formation of molecular states.[22] Bonding orbitals have a large amplitude in the barrier and thus add a large contribution from the GaAs to the overall hole g factor. This adds a positive component to the otherwise negative heavy-hole g factor and suppresses the Zeeman splitting on resonance. In contrast, antibonding states suppress the contributions from the tail of the wave function in the barrier, enhance the negative g factor, and result in increased Zeeman splitting on resonance. In addition to providing a tool for electrical modulation of g factors, the resonant changes in g factor can also be used to measure the orbital character of the delocalized molecular states and confirm the molecular-orbital filling model presented in Sec. III.

Before presenting the resonant changes in the g factor for the X^{2+} states, we first briefly review how resonant changes in g factor appear in magneto-PL experiments on the neutral exciton and positive trion. In Fig. 14(a) we plot the Zeeman splitting at $B=6$ T of neutral exciton and positive trion PL lines from a single QDM with a 2 nm barrier. For the neutral exciton (X^0), we plot PL lines that originate in both the low- and the high-energy molecular orbitals. The low-energy molecular orbital is observed to have a resonant decrease in Zeeman splitting, which indicates that it has bonding orbital character. The positive trion (X^+) PL, which also comes from the low-energy molecular orbital, displays a similar resonant decrease in the Zeeman splitting indicative of bonding orbital character. In contrast, the high-energy molecular orbital of the neutral exciton is found to have a resonant increase in Zeeman splitting as a result of its antibonding character. The resonances reach their extreme values at the electric field of maximum anticrossing for each state (F_{X^0} and F_{h^+}).

In Fig. 14(b) we plot the Zeeman splitting for the three pairs of X^{2+} transitions described in Eq. (9), which are also the three pairs of photoluminescence lines clearly visible in Fig. 11(a). The X^{2+} transitions are measured for the same QDM as the X^0 and X^+ displayed in Fig. 14(a). By comparing the observed X^{2+} PL lines with the lines in the calculated spectra (Fig. 11), we determine that the initial state for all

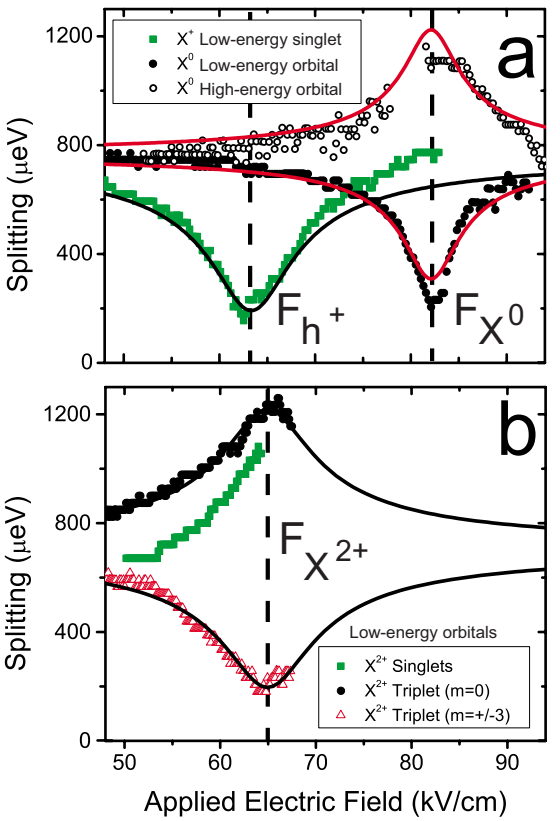

FIG. 14. (Color online) Measured Zeeman splitting at $B=6$ T from a QDM with 2 nm barrier. (a) PL transitions involving the molecular orbitals of the neutral exciton and positive trion. (b) The three X^{2+} PL states in Eq. (9). The solid lines are fits to the data using Eq. (10) as described in the text.

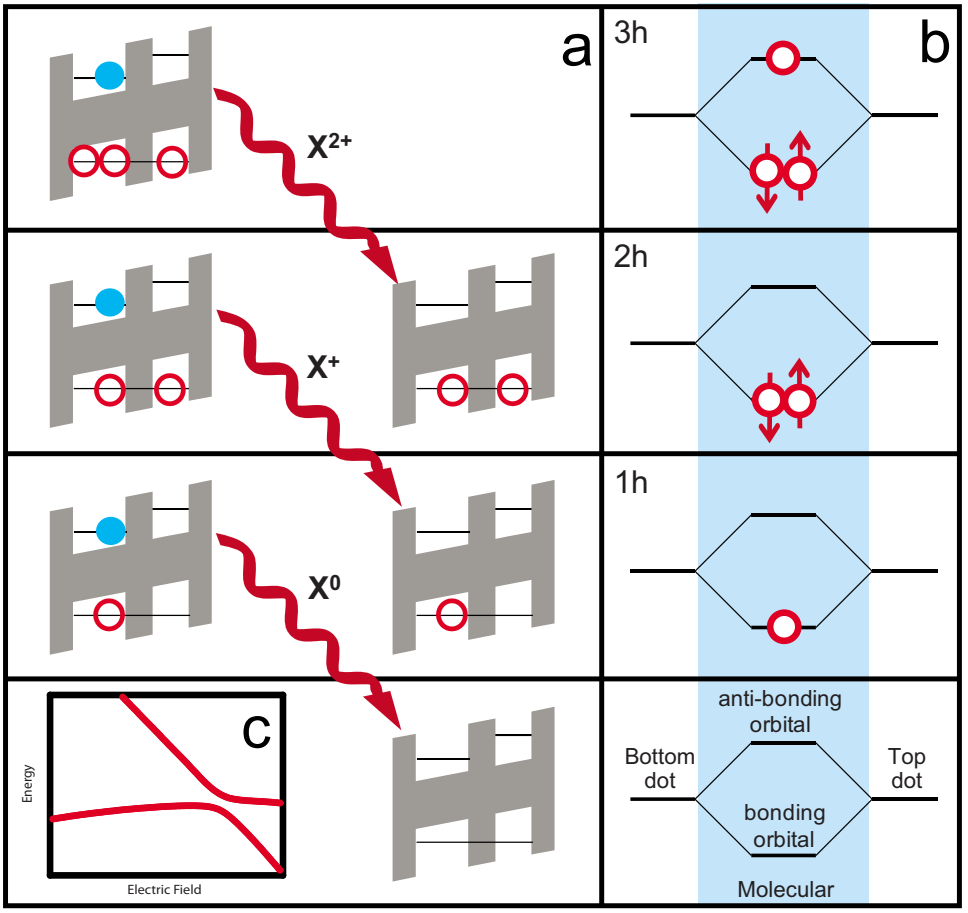

FIG. 15. (Color online) (a) Band schematics for QDMs charged with one, two, or three excess holes. (b) Lowest-energy filling of the molecular orbitals that form on resonance. (c) PL of a neutral exciton in a QDM with holes tunneling through a 2 nm barrier, which illustrates the formation of molecular orbitals at the anticrossing.

three transitions is the lower-energy molecular branch. The PL lines resulting from recombination to the singlet and triplet with total angular momentum zero ($m=0$) have a resonant *increase* in splitting, reaching a maximum splitting of about 1.2 meV. The photoluminescence lines resulting from recombination to the triplets with total angular momentum of ± 3 reach a minimum splitting of about 0.2 meV. All three curves reach extreme values of the Zeeman splitting at approximately 65 kV/cm, which is the point of maximum anticrossing for the optically excited state ($F_{X^{2+}}$).

We first consider the transition to the $m=0$ triplet state:

$$\alpha\begin{pmatrix}\uparrow,0\\ \Downarrow\Uparrow,\Downarrow\end{pmatrix}+\beta\begin{pmatrix}\uparrow,0\\ \Downarrow,\Downarrow\Uparrow\end{pmatrix}\rightarrow\begin{pmatrix}0,0\\ \Downarrow,\Uparrow\end{pmatrix}_T.$$

Because the h^{2+} (optical ground) state has two oppositely oriented spins, it has no Zeeman splitting. The observed Zeeman splitting of the photoluminescence lines must therefore depend only on the Zeeman splitting in the X^{2+} (optically excited) state (see Fig. 13). The resonant enhancement of the Zeeman splitting is the signature of an antibonding molecular orbital, which validates the molecular-orbital filling model presented above.

In Fig. 15 we show the excitonic transitions and molecular-orbital filling for QDMs charged with one, two, and three holes. Bonding and antibonding orbitals are constructed from the states of a single tunneling hole. The bonding configuration has lowest energy. For the initial state of the neutral exciton and the final state of the positive trion, the orbitals must be filled with one hole. The lowest-energy configuration places this hole in the bonding orbital. We observe bonding orbital character for low-energy molecular branches in the neutral and positive trion configurations for this QDM. For the initial state of the X^{2+} recombination, the orbitals must be filled with three holes. The lowest-energy configuration fills the lowest-energy bonding orbital with two spin-paired holes. The remaining unpaired hole goes in the higher-energy antibonding orbital. The resonant change in the g factor comes only from this single unpaired hole. Thus, the lower-energy molecular branch in the optically excited state of a doubly charged QDM with 2 nm tunnel barrier displays antibonding character.

The resonant contribution of the barrier to the g factors of molecular states is captured in the Hamiltonian [Eq. (8)] by the term g'. g' is a positive number since it originates in the g factor of a heavy hole in GaAs. The sign of g' at each matrix element in the Zeeman Hamiltonian is determined by the spin orientation of the tunneling hole. If the tunneling hole has spin up, the additional matrix element would be $-g'$ because of the minus sign for holes in Eq. (6). When we include the additional sign change from the antisymmetrization of the three-particle basis states, the term that appears in the Hamiltonian is $+g'$.

Using Eq. (8), we can derive an expression for the resonant change in g factor,

$$g(F) = g_e + g_h + \frac{2tg'}{\sqrt{e^2d^2(F - F_{X^{2+}})^2 + 4t^2}}, \qquad (10)$$

where $F_{X^{2+}}$ is the electric field of the anticrossing for the X^{2+} optically excited state. g_e+g_h is determined by the asymptotic value of the Zeeman splitting at low applied electric fields. The asymptotic value of the splitting, 0.707 meV, corresponds to a total transition g factor of −2.035, which is quite similar to the total transition g factor found for the neutral exciton and positive trion (−2.145). t=0.86 meV, d =0.39 meV cm/kV, and $F_{X^{2+}}$=64.94 kV/cm are determined by the measured spectra at zero magnetic field. g' is the only unknown parameter. Treating g' as a free parameter, we fit Eq. (10) to the data shown in Fig. 14(b). We find g' =1.47, which is quite similar to the results found for X^0 (1.32) and X^+ (1.65). This fit is shown by the black line in Fig. 14(b).

The singlet states have the same spin orientation as the m=0 triplet states. As a result, the observed enhancement of the Zeeman splitting for recombination to the singlet states in Fig. 14 is qualitatively similar to the m=0 triplet states. However, there is a quantitative offset for the singlet state. Since the singlet and the m=0 triplet have the same initial state, this offset must be due to differences in the final state. Although both the singlet and the m=0 triplet states have two oppositely oriented spins, the $\binom{0,0}{\Downarrow,\Uparrow}_S$ singlet state is tunnel coupled to both $\binom{0,0}{\Downarrow\Uparrow,0}$ and $\binom{0,0}{0,\Downarrow\Uparrow}$, while the m=0 triplet state remains uncoupled. The observed offset may be due to the proximity of these additional anticrossings, one of which occurs at approximately 45 kV/cm.

In contrast to the singlet and m=0 triplet, recombination to the $m=\pm 3$ triplet states exhibits a resonant decrease in Zeeman splitting. This resonant decrease results from the incomplete cancellation of hole g factors in the initial (optically excited) and final (optical ground) states. From Eq. (9) we see that the transition g factor for recombination to the $m=\pm 3$ triplet states is given by $(g_e-g_h)-(-2g_h)=(g_e+g_h)$. The resonant enhancement of the g factor from the unpaired hole in the antibonding orbital effectively increases the magnitude of g_h in the initial state but has no effect on $-2g_h$ in the final state because the two parallel holes do not tunnel. As a result, the Zeeman splitting of the transition on resonance is given by $[g_e-(g_h-g')]-(-2g_h)=(g_e+g_h+g')$. Because g_e and g_h are negative and g' is positive, the observed Zeeman splitting is reduced by g'. The resonant contribution of the barrier to the Zeeman splitting of the $m=\pm 3$ triplet state is depicted in Fig. 13. The Zeeman splitting of the m $=\pm 3$ triplet state in Fig. 14 is fitted by an equation analogous to Eq. (10) using the same parameters found for the m=0 triplet state.

The full Hamiltonian for the X^{2+} state [Eq. (8)] has net tunneling matrix elements of $t\pm g'$. Because the sign of g' depends on the spin orientation of the tunneling hole, the magnitude of the net tunneling matrix element is spin dependent. The sign of t can be controlled by changing the thickness of the barrier.[23]

C. QDMs charged with two electrons

Our discussion of applied magnetic fields has focused on QDMs charged with two resident holes. We have also studied QDMs charged with two resident electrons in a magnetic field. Doubly negatively charged QDMs exhibit a Zeeman splitting that can be described with equations analogous to Eqs. (7) and (8). However, doubly negatively charged QDMs do not exhibit any resonant change in Zeeman splitting as a function of applied electric field. Plots analogous to Fig. 14 show simply a flat horizontal line at the Zeeman splitting given by the sum of the g factors for the electron and hole. The amplitude of the wave function in the barrier is larger for electron tunneling than for hole tunneling (at similar barrier thicknesses). However, the g factor for electrons in bulk GaAs is −0.44. This value is quite similar to the g factor for electrons confined in the dots (∼−0.7). Consequently, the resonant change in electron wave-function amplitude in the barrier does not induce a significant change in the net g factor. We therefore observe no resonant change in Zeeman splitting and find g'=0 for QDMs charged with two resident electrons.

VII. SUMMARY

Doubly charged quantum dot molecules are important elements in many theoretical proposals for the development of spin-based quantum information processing devices. Before discussing the implications for specific proposals, it will be helpful to summarize the results presented so far. For simplicity, we will continue to discuss QDMs charged with two excess holes.

InAs QDs separated by a GaAs barrier are grown using molecular-beam epitaxy. The lowest confined energy levels in each dot are generally not at equal energy but can be tuned into resonance by an applied electric field. If the QDM is charged with two excess holes, the holes can be distributed between the two dots. If both holes are in the same dot, they must be in a spin singlet. Because tunneling is a spin-preserving process, only the spin singlet configuration of one hole in each dot can tunnel couple with the states that have two holes in a single dot. Triplet configurations cannot participate in these tunnel couplings. As a result, singlet and triplet states are separated by a kinetic exchange energy. The proximity of multiple singlet anticrossings can induce a kinetic exchange energy separating singlet and triplet states over a wide range of electric fields.

The optically excited state of a doubly charged QDM consists of three holes and one electron. Because we restrict our analysis to include only the lowest single-particle states (i.e., the atomic s-shell state), there must always be two spin-paired holes in one dot and a single unpaired hole in the second dot. When the single hole is located in the same dot as the electron, the electron-hole exchange splits the state energies. The anticrossing that arises from tunneling of a hole between the two dots occurs at a different electric field from anticrossings in the optical ground state because of Coulomb interactions.

Resonant tunneling of holes between the two dots results in the formation of molecular orbitals. These orbitals can be understood by constructing the symmetric and antisymmetric combinations of basis states with a single hole localized in one dot or the other. The symmetric and antisymmetric mo-

lecular orbitals have bonding and antibonding characters, respectively. The bonding orbital has the lowest energy, though in the case of holes this is true only for barrier thickness of less than 3 nm.[23] In the optically excited state, the molecular orbitals are filled with three holes. The lowest-energy configuration has two spin-paired holes in the low-energy bonding state and one unpaired hole in the antibonding orbital. As a result, the low-energy molecular branch exhibits antibonding properties in magnetophotoluminescence experiments.

The resonant formation of bonding and antibonding orbitals results in wave functions with a large amplitude in the GaAs barrier. This results in a resonant decrease or increase, respectively, in the heavy-hole g factor. This creates a spin-dependent tunneling barrier that manifests as a resonant increase or decrease of the Zeeman splitting in photoluminescence lines.

We have demonstrated above that the analysis presented here applies equally well to QDMs containing two excess electrons or two excess holes. Nevertheless, there are several differences that we should emphasize. Because of the difference in effective mass, electrons tunnel more easily and have anticrossing energy gaps roughly an order of magnitude larger than that observed for holes tunneling through a barrier of identical thickness.[17] The relatively thin barriers used to study coherent hole tunneling (2–6 nm) result in electron states that are strongly delocalized at all values of the applied electric field. Consequently, we typically study electron tunneling in samples with a thicker barrier (10–16 nm). This thicker barrier results in larger linewidths for indirect transitions as a result of spectral wandering with slight variations in applied electric field. The typical tunneling rates observed for electrons suppress the observation of spin fine structure from electron-hole exchange. Additionally, no resonant change in g factor due to delocalized wave functions has been observed for electron tunneling. Unlike electrons, holes have a strong spin-orbit interaction that can reverse the energy ordering of bonding and antibonding molecular orbitals.[23,31–34]

VIII. IMPLICATIONS FOR QUANTUM INFORMATION

One of the earliest proposals for the implementation of quantum information processing in the solid state was to use a single electron confined to a single QD as the qubit.[2] Two-qubit operations were to be executed by lowering the potential barrier between neighboring dots to allow exchange operations to take place. In self-assembled QDs we have an alternative method for controlling exchange interactions between spins in proximate QDs by tuning the energy levels of the two dots in and out of resonance. This tuning varies the magnitude of the kinetic exchange interaction, which results in a tunable energy separation between singlet and triplet states. In an alternative configuration, the singlet and triplet states of a doubly charged QDM could be used as the basis states for a qubit.[54] Recent experiments in electrostatically defined QDs have demonstrated Rabi oscillations in the singlet-triplet basis[3] and measured coherence times of up to 10 μs.[3,6] Here we demonstrate electrical control over the energy separation of singlet and triplet states and discuss how sample structure can also be used to control the range over which singlet and triplet states remain separated. The results are a crucial element for the design of QDMs that can be coupled to superconducting cavities to enable long-range quantum gate operations.[55]

Of particular value in this paper is the analysis of coupling mechanisms in both the optical ground and the optically excited states. This analysis lays the foundation for the design of hybrid schemes that utilize both electrical and optical manipulations of spins. Optical manipulation of qubits can be substantially faster than electrical gating. Recently, Saikin *et al.*[56] proposed a mechanism to optically generate entanglement between two electron spins confined in a QDM by using Coulomb interactions in the optically excited states. Other methods of coherent control have also been proposed.[57–60] The results presented here are crucial to the sample design and implementation of such proposals.

Finally, we point out that the resonant contribution of the barrier to the g factor for molecular orbitals creates a spin-dependent tunnel barrier. This provides another powerful tool for the design of spin manipulation protocols in QDMs. At present this effect has only been observed for hole tunneling, but there are many reasons to consider hole spins as the fundamental unit for quantum information processing.[61,62]

ACKNOWLEDGMENTS

The authors acknowledge financial support from NSA/USARO and ONR. I.V.P. and M.F.D. acknowledge support from NRC/NRL.

APPENDIX

In the main text we have described the states of doubly charged QDMs using atomiclike basis states that account for the possible spatial distributions and spin orientations. Here we present a theoretically rigorous definition of the basis states and the Hamiltonians. We will present only the states of QDMs charged with two holes; the case of two electrons is analogous.

We continue to consider only the range of applied electric fields where the two hole levels are close to resonance but the electron energies are quite different. The electron is therefore confined to its energetic ground state $\varphi_B^e(\mathbf{r})$ ($|B^e\rangle$), which corresponds to dominant localization of the electron in the bottom QD. The electron spin-wave function is given by $|\alpha_e\rangle=|S_z,-1/2\rangle$, $|\beta_e\rangle=|S_z,+1/2\rangle$. The spatial basis states for the holes are the two lowest orthonormal states $\varphi_B^h(\mathbf{r})$ and $\varphi_T^h(\mathbf{r})$ ($|B^h\rangle$ and $|T^h\rangle$), which are localized primarily in the bottom or in the top QD. The relative energy of states is tuned by the applied electric field F. We take the zero of electric field to be when the two hole states would be degenerate in energy in the absence of coupling between the dots. The heavy-hole spin function ($J=3/2$, $J_z=\pm 3/2$) is taken to be a fermion with the pseudospin 1/2. To avoid phase multipliers in the pseudospin representation,[63,64] its projections are $|\alpha_h\rangle\equiv|-1/2\rangle=|J_z,+3/2\rangle$ and $|\beta_h\rangle\equiv|+1/2\rangle=|J_z,-3/2\rangle$. We construct the many-body basis states from antisymmetrized products of these single-particle states. For two-

particle hole spin states, we use the orthogonal singlet and triplet spin-wave functions: $|s_{ij}\rangle=2^{-1/2}(|\beta_i\rangle|\alpha_j\rangle-|\alpha_i\rangle|\beta_j\rangle)$, $|\tau_{ij}^0\rangle=2^{-1/2}(|\beta_i\rangle|\alpha_j\rangle+|\alpha_i\rangle|\beta_j\rangle)$, $|\tau_{ij}^{(+1)}\rangle=|\beta_i\rangle|\beta_j\rangle$, and $|\tau_{ij}^{(-1)}\rangle=|\alpha_i\rangle|\alpha_j\rangle$.

We consider the electrons to be distinguishable from the holes. In the envelope function approximation, the many-particle Hamiltonian of the QDMs consists of three parts:

$$\hat{H}=\sum_l \hat{\mathbf{h}}_l^a+\sum_{l,m} V_C(|\mathbf{r}_{al}-\mathbf{r}_{bm}|)+\hat{H}_{\text{exch}}^{\text{e-h}}, \tag{A1}$$

where $a,b=e$ or h. The first term gives the single-particle electron and hole QD Hamiltonians, the second term describes the Coulomb interactions between particles, and the third term explicitly includes the short-range electron-hole exchange. The single-particle Hamiltonians have the following matrix elements: $\langle B^a|\hat{\mathbf{h}}^a|B^a\rangle=\varepsilon_a$, $\langle T^h|\hat{\mathbf{h}}^h|T^h\rangle=\varepsilon_h-edF$, and $\langle B^h|\hat{\mathbf{h}}^h|T^h\rangle=-t$, where ε_a is the electron or hole confinement energy in single QD, and t is the hole-tunneling rate. The Coulomb part of the many-particle Hamiltonian generates eight Coulomb integrals: $V_{ijkl}^{ab}=\int\int d\mathbf{r}d\mathbf{r}'|\mathbf{r}-\mathbf{r}'|^{-1}\varphi_i^{a*}(\mathbf{r})\varphi_j^a(\mathbf{r})\varphi_k^{b*}(\mathbf{r}')\varphi_l^b(\mathbf{r}')$, where $i,j,k,l=B$ or T. For direct Coulomb integrals we use abbreviated notations: $V_{ik}^{ab}\equiv V_{iikk}^{ab}$. The short-range electron-hole exchange is determined using the effective Hamiltonian[64]

$$\hat{H}_{\text{exch}}^{\text{e-h}}=A\sum_{i,j}\delta(\mathbf{r}_{ei}-\mathbf{r}_{hj})\hat{\sigma}_{ez}^{(i)}\hat{\sigma}_{hz}^{(j)}, \tag{A2}$$

where A is a coupling constant and $\hat{\sigma}_{e(h)z}$ are Pauli matrices. z is the growth direction, which is the strongest confinement for electrons and holes. The electron-hole exchange is described by the parameter $J_{ij}^{\text{e-h}}=\int\int d\mathbf{r}|\varphi_B^e(\mathbf{r})|^2\varphi_i^{h*}(\mathbf{r})\varphi_j^h(\mathbf{r})$.

For the experiments discussed in this paper, many terms are sufficiently small that they can be neglected. The absolute values of the Coulomb terms V_{BBBB}^{ab} are 10–20 meV, comparable to the separation of single-particle energy levels. However, these terms always appear on the diagonal of many-body Hamiltonians as differences that represent the energy shift between two spatial configurations of charges. Because they arise from differences, the typical magnitude of the physical parameters in the Hamiltonians is 1–5 meV. Typical values for the hole-tunneling rate (t) and intradot electron-hole exchange ($J^{\text{e-h}}\equiv J_{BB}^{\text{e-h}}$) are at least 0.2 meV. The terms $J_{TT}^{\text{e-h}}$ and V_{BTBT}^{hh} are responsible for the exchange energies between particles in different QDs and can be neglected because they are less than 1 μeV. V_{BBBT}^{ab} and $J_{BT}^{\text{e-h}}$ are off-diagonal Coulomb and exchange matrix elements responsible for small corrections (<10 μeV) to tunneling rates and can be similarly neglected.

The many-body basis states for the h^{2+} state, which has only two holes, are

$$|1_{h^{2+}}\rangle=|B_1^hB_2^h\rangle|s_{12}\rangle=\begin{pmatrix}0,0\\ \Downarrow\Uparrow,0\end{pmatrix}_S,$$

$$|2_{h^{2+}}\rangle=\left|\frac{B_1^hT_2^h+T_1^hB_2^h}{\sqrt{2}}\right\rangle|s_{12}\rangle=\begin{pmatrix}0,0\\ \Downarrow,\Uparrow\end{pmatrix}_S,$$

$$|3_{h^{2+}}\rangle=\left|\frac{B_1^hT_2^h-T_1^hB_2^h}{\sqrt{2}}\right\rangle|\tau_{12}^0\rangle=\begin{pmatrix}0,0\\ \Downarrow,\Uparrow\end{pmatrix}_T,$$

$$|4_{h^{2+}}\rangle=\left|\frac{B_1^hT_2^h-T_1^hB_2^h}{\sqrt{2}}\right\rangle|\tau_{12}^{(+1)}\rangle=\begin{pmatrix}0,0\\ \Downarrow,\Downarrow\end{pmatrix}_T,$$

$$|5_{h^{2+}}\rangle=\left|\frac{B_1^hT_2^h-T_1^hB_2^h}{\sqrt{2}}\right\rangle|\tau_{12}^{(-1)}\rangle=\begin{pmatrix}0,0\\ \Uparrow,\Uparrow\end{pmatrix}_T,$$

$$|6_{h^{2+}}\rangle=|T_1^hT_2^h\rangle|s_{12}\rangle=\begin{pmatrix}0,0\\ 0,\Downarrow\Uparrow\end{pmatrix}_S. \tag{A3}$$

In this basis, the Hamiltonian ($\hat{H}=\hat{\mathbf{h}}_1^h+\hat{\mathbf{h}}_2^h+|\mathbf{r}_{h2}-\mathbf{r}_{h1}|^{-1}$) is represented by the matrix of Eq. (7), with energies referenced to $H_{22}=2\varepsilon_h+V_{BBTT}^{hh}$. In Eq. (7) we have used the definitions

$$\Gamma_2=V_{BBBB}^{hh}-V_{BBTT}^{hh},$$

$$\Gamma_3=V_{TTTT}^{hh}-V_{BBTT}^{hh}. \tag{A4}$$

The triplet states are degenerate at zero magnetic field and decoupled from the singlet states and can thus be removed from the matrix. The singlet eigenstates can be calculated from the determinant of the remaining 3×3 matrix.

The many-body basis states for the X^{2+} state, which has one electron and three holes, are

$$|1_{X^{2+}}\rangle=\frac{|B^e,\beta^e\rangle}{\sqrt{3}}[|B_1B_2T_3\rangle|s_{12},\beta_3\rangle+|B_1T_2B_3\rangle|s_{31},\beta_2\rangle+|T_1B_2B_3\rangle|s_{23},\beta_1\rangle]=\begin{pmatrix}\uparrow,0\\ \Downarrow\Uparrow,\Downarrow\end{pmatrix},$$

$$|2_{X^{2+}}\rangle=\frac{|B^e,\alpha^e\rangle}{\sqrt{3}}[|B_1B_2T_3\rangle|s_{12},\alpha_3\rangle+|B_1T_2B_3\rangle|s_{31},\alpha_2\rangle+|T_1B_2B_3\rangle|s_{23},\alpha_1\rangle]=\begin{pmatrix}\downarrow,0\\ \Downarrow\Uparrow,\Uparrow\end{pmatrix},$$

$$|3_{X^{2+}}\rangle=\frac{|B^e,\beta^e\rangle}{\sqrt{3}}[|B_1B_2T_3\rangle|s_{12},\alpha_3\rangle+|B_1T_2B_3\rangle|s_{31},\alpha_2\rangle+|T_1B_2B_3\rangle|s_{23},\alpha_1\rangle]=\begin{pmatrix}\uparrow,0\\ \Downarrow\Uparrow,\Uparrow\end{pmatrix},$$

$$|4_{X^{2+}}\rangle=\frac{|B^e,\alpha^e\rangle}{\sqrt{3}}[|B_1B_2T_3\rangle|s_{12},\beta_3\rangle+|B_1T_2B_3\rangle|s_{31},\beta_2\rangle+|T_1B_2B_3\rangle|s_{23},\beta_1\rangle]=\begin{pmatrix}\downarrow,0\\ \Downarrow\Uparrow,\Downarrow\end{pmatrix},$$

$$|5_{X^{2+}}\rangle=\frac{|B^e,\beta^e\rangle}{\sqrt{3}}[|T_1T_2B_3\rangle|s_{12},\beta_3\rangle+|T_1B_2T_3\rangle|s_{31},\beta_2\rangle+|B_1T_2T_3\rangle|s_{23},\beta_1\rangle]=\begin{pmatrix}\uparrow,0\\ \Downarrow,\Downarrow\Uparrow\end{pmatrix},$$

$$|6_{X^{2+}}\rangle = \frac{|B^e,\alpha^e\rangle}{\sqrt{3}}[|T_1T_2B_3\rangle|s_{12},\alpha_3\rangle + |T_1B_2T_3\rangle|s_{31},\alpha_2\rangle + |B_1T_2T_3\rangle|s_{23},\alpha_1\rangle] = \begin{pmatrix}\downarrow,0\\ \Uparrow,\Downarrow\Uparrow\end{pmatrix},$$

$$|7_{X^{2+}}\rangle = \frac{|B^e,\beta^e\rangle}{\sqrt{3}}[|T_1T_2B_3\rangle|s_{12},\alpha_3\rangle + |T_1B_2T_3\rangle|s_{31},\alpha_2\rangle + |B_1T_2T_3\rangle|s_{23},\alpha_1\rangle] = \begin{pmatrix}\uparrow,0\\ \Uparrow,\Downarrow\Uparrow\end{pmatrix},$$

$$|8_{X^{2+}}\rangle = \frac{|B^e,\alpha^e\rangle}{\sqrt{3}}[|T_1T_2B_3\rangle|s_{12},\beta_3\rangle + |T_1B_2T_3\rangle|s_{31},\alpha_2\rangle + |B_1T_2T_3\rangle|s_{23},\beta_1\rangle] = \begin{pmatrix}\downarrow,0\\ \Downarrow,\Downarrow\Uparrow\end{pmatrix}. \quad \text{(A5)}$$

The Hamiltonian is $\hat{H}=\hat{H}^{(1)}+\hat{V}^C+\hat{H}^{\text{e-h}}_{\text{exch}}$, where

$$\hat{H}^{(1)} = \hat{\mathbf{h}}_1^e + \sum_{i=1}^{3}\hat{\mathbf{h}}_i^h,$$

$$\hat{V}^C = -|\mathbf{r}_e-\mathbf{r}_{h1}|^{-1} - |\mathbf{r}_e-\mathbf{r}_{h2}|^{-1} - |\mathbf{r}_e-\mathbf{r}_{h3}|^{-1} + |\mathbf{r}_{h1}-\mathbf{r}_{h2}|^{-1} + |\mathbf{r}_{h1}-\mathbf{r}_{h3}|^{-1} + |\mathbf{r}_{h2}-\mathbf{r}_{h3}|^{-1}, \quad \text{(A6)}$$

$$\hat{H}^{\text{e-h}}_{\text{exch}} = A\sum_{i=1}^{3}\delta(\mathbf{r_e}-\mathbf{r_{hi}})\hat{\sigma}_{ez}\hat{\sigma}_{zi}. \quad \text{(A7)}$$

The full Hamiltonian is given in Eq. (8), where we reference the energies to $\Omega=\varepsilon_e+3\varepsilon_h-V^{eh}_{BBBB}+V^{hh}_{TTTT}-2V^{eh}_{BBTT}+2V^{hh}_{BBTT}$, which is the energy of the states with two holes in the top dot and one hole in the bottom dot, neglecting the Stark shift and electron-hole exchange. $\Gamma_4=-V^{eh}_{BBBB}+V^{hh}_{BBBB}-V^{hh}_{TTTT}+V^{eh}_{BBTT}$ captures the energy shift of moving one hole from the top to the bottom dot. The eigenenergies of Eq. (8) are

$$E = \Omega + 1/2[edF \pm J^{\text{e-h}} + \Gamma_4 \mp \sqrt{edF^2 \pm 2edFJ^{\text{e-h}} + (J^{\text{e-h}})^2 + 4t^2_{X^{2+}} - 2edF\Gamma_4 \mp 2J^{\text{e-h}}\Gamma_4 + \Gamma_4^2}]. \quad \text{(A8)}$$

*Present address: University of Delaware, Newark, Delaware, USA; doty@udel.edu

[1] D. D. Awschalom, D. Loss, and N. Samarth, *Semiconductor Spintronics and Quantum Computation* (Springer, New York, 2002).

[2] D. Loss and D. P. DiVincenzo, Phys. Rev. A **57**, 120 (1998).

[3] J. R. Petta, A. C. Johnson, J. M. Taylor, E. A. Laird, A. Yacoby, M. D. Lukin, C. M. Marcus, M. P. Hanson, and A. C. Gossard, Science **309**, 2180 (2005).

[4] A. C. Johnson, J. R. Petta, J. M. Taylor, A. Yacoby, M. D. Lukin, C. M. Marcus, M. P. Hanson, and A. C. Gossard, Nature (London) **435**, 925 (2005).

[5] F. H. L. Koppens, C. Buizert, K. J. Tielrooij, I. T. Vink, K. C. Nowack, T. Meunier, L. P. Kouwenhoven, and L. M. K. Vandersypen, Nature (London) **442**, 766 (2006).

[6] F. H. L. Koppens, J. A. Folk, J. M. Elzerman, R. Hanson, L. H. W. v. Beveren, I. T. Vink, H. P. Tranitz, W. Wegscheider, L. P. Kouwenhoven, and L. M. K. Vandersypen, Science **309**, 1346 (2005).

[7] K. C. Nowack, F. H. L. Koppens, Y. V. Nazarov, and L. M. K. Vandersypen, Science **318**, 1430 (2007).

[8] X. D. Xu, Y. W. Wu, B. Sun, Q. Huang, J. Cheng, D. G. Steel, A. S. Bracker, D. Gammon, C. Emary, and L. J. Sham, Phys. Rev. Lett. **99**, 097401 (2007).

[9] M. E. Ware, E. A. Stinaff, D. Gammon, M. F. Doty, A. S. Bracker, D. Gershoni, V. L. Korenev, S. C. Badescu, Y. Lyanda-Geller, and T. L. Reinecke, Phys. Rev. Lett. **95**, 177403 (2005).

[10] Y. Wu, E. D. Kim, X. Xu, J. Cheng, D. G. Steel, A. S. Bracker, D. Gammon, S. E. Economou, and L. J. Sham, Phys. Rev. Lett. **99**, 097402 (2007).

[11] S. E. Economou and T. L. Reinecke, Phys. Rev. Lett. **99**, 217401 (2007).

[12] M. Atature, J. Dreiser, A. Badolato, A. Hogele, K. Karrai, and A. Imamoglu, Science **312**, 551 (2006).

[13] M. Bayer, P. Hawrylak, K. Hinzer, S. Fafard, M. Korkusinski, Z. R. Wasilewski, O. Stern, and A. Forchel, Science **291**, 451 (2001).

[14] H. J. Krenner, M. Sabathil, E. C. Clark, A. Kress, D. Schuh, M. Bichler, G. Abstreiter, and J. J. Finley, Phys. Rev. Lett. **94**, 057402 (2005).

[15] G. Ortner, M. Bayer, Y. Lyanda-Geller, T. L. Reinecke, A. Kress, J. P. Reithmaier, and A. Forchel, Phys. Rev. Lett. **94**, 157401 (2005).

[16] E. A. Stinaff, M. Scheibner, A. S. Bracker, I. V. Ponomarev, V. L. Korenev, M. E. Ware, M. F. Doty, T. L. Reinecke, and D. Gammon, Science **311**, 636 (2006).

[17] A. S. Bracker, M. Scheibner, M. F. Doty, E. A. Stinaff, I. V. Ponomarev, J. C. Kim, L. J. Whitman, T. L. Reinecke, and D. Gammon, Appl. Phys. Lett. **89**, 233110 (2006).

[18] H. J. Krenner, E. C. Clark, T. Nakaoka, M. Bichler, C. Scheurer, G. Abstreiter, and J. J. Finley, Phys. Rev. Lett. **97**, 076403 (2006).

[19] T. Nakaoka, E. C. Clark, H. J. Krenner, M. Sabathil, M. Bichler, Y. Arakawa, G. Abstreiter, and J. J. Finley, Phys. Rev. B **74**, 121305 (2006).

[20] M. Scheibner, I. V. Ponomarev, E. A. Stinaff, M. F. Doty, A. S. Bracker, C. S. Hellberg, T. L. Reinecke, and D. Gammon, Phys. Rev. Lett. **99**, 197402 (2007).

[21] M. Scheibner, M. F. Doty, I. V. Ponomarev, A. S. Bracker, E. A. Stinaff, V. L. Korenev, T. L. Reinecke, and D. Gammon, Phys.

Rev. B **75**, 245318 (2007).
[22] M. F. Doty, M. Scheibner, I. V. Ponomarev, E. A. Stinaff, A. S. Bracker, V. L. Korenev, T. L. Reinecke, and D. Gammon, Phys. Rev. Lett. **97**, 197202 (2006).
[23] M. F. Doty, J. I. Climente, M. Korkusinski, M. Scheibner, A. S. Bracker, P. Hawrylak, and D. Gammon, arXiv:0804.3097 (unpublished).
[24] S. Faelt, M. Atature, H. E. Tureci, Y. Zhao, A. Badolato, and A. Imamoglu, Phys. Rev. Lett. **100**, 106401 (2008).
[25] M. Scheibner, M. Yakes, A. S. Bracker, I. V. Ponomarev, M. F. Doty, C. S. Hellberg, L. J. Whitman, T. L. Reinecke, and D. Gammon, Nat. Phys. **4**, 291 (2008).
[26] L. Robledo, J. Elzerman, G. Jundt, M. Atature, A. Hogele, S. Falt, and A. Imamoglu, Science **320**, 772 (2008).
[27] Y. B. Lyanda-Geller, T. L. Reinecke, and M. Bayer, Phys. Rev. B **69**, 161308(R) (2004).
[28] J. M. Villas-Boas, A. O. Govorov, and S. E. Ulloa, Phys. Rev. B **69**, 125342 (2004).
[29] D. Bellucci, F. Troiani, G. Goldoni, and E. Molinari, Phys. Rev. B **70**, 205332 (2004).
[30] B. Szafran, T. Chwiej, F. M. Peeters, S. Bednarek, J. Adamowski, and B. Partoens, Phys. Rev. B **71**, 205316 (2005).
[31] G. Bester, J. Shumway, and A. Zunger, Phys. Rev. Lett. **93**, 047401 (2004).
[32] G. Bester, A. Zunger, and J. Shumway, Phys. Rev. B **71**, 075325 (2005).
[33] W. Jaskolski, M. Zielinski, and G. W. Bryant, Acta Phys. Pol. A **106**, 193 (2004).
[34] W. Jaskolski, M. Zielinski, G. W. Bryant, and J. Aizpurua, Phys. Rev. B **74**, 195339 (2006).
[35] I. V. Ponomarev, M. Scheibner, E. A. Stinaff, A. S. Bracker, M. F. Doty, S. C. Badescu, M. E. Ware, V. L. Korenev, T. L. Reinecke, and D. Gammon, Phys. Status Solidi B **243**, 3869 (2006).
[36] M. Z. Maialle and M. H. Degani, Phys. Rev. B **76**, 115302 (2007).
[37] B. Szafran and F. M. Peeters, Phys. Rev. B **76**, 195442 (2007).
[38] Z. R. Wasilewski, S. Fafard, and J. P. McCaffrey, J. Cryst. Growth **201–202**, 1131 (1999).
[39] J. M. Garcia, G. Medeiros-Ribeiro, K. Schmidt, T. Ngo, J. L. Feng, A. Lorke, J. Kotthaus, and P. M. Petroff, Appl. Phys. Lett. **71**, 2014 (1997).
[40] Note that the electric field is applied to operate the diode in "reverse bias," which prevents the QDs from being flooded with electrons or holes from the substrate and enables controllable charging.
[41] P. Fazekas, *Series in Modern Condensed Matter Physics*, Lecture Notes on Electron Correlation and Magnetism (World Scientific, Singapore, 1999).
[42] G. Burkard, D. Loss, and D. P. DiVincenzo, Phys. Rev. B **59**, 2070 (1999).
[43] Note that this change in sign applies to the term t. An additional sign change for the off-diagonal matrix elements responsible for tunneling occurs when we move from the X^- and e^{2-} Hamiltonians to the X^{2-} Hamiltonian as a result of antisymmetrization of the three-particle wave functions.
[44] J. I. Climente, M. Korkusinski, and P. Hawrylak (unpublished).
[45] Interactions with other charges confined in the dots can introduce an additional small change in the tunneling rate between different excitonic species (which have different numbers of spectator charges) (Ref. 16). We have neglected these Coulomb corrections to the tunneling rate, which are generally negligible unless the tunnel barrier is quite thin. Note also that the tunneling matrix element now appears as $-t$ rather than t, as it does in Eq. (1). This sign change is a result of the proper antisymmetrization of the basis states as defined in the Appendix. Because of the antisymmetrization, tunneling matrix elements in the Hamiltonians for the X^{2-} and X^{2+} states pick up an additional minus sign relative to the e^{2-} and h^{2+} state Hamiltonians. The sign of the tunneling matrix element does not change the calculation of energy levels at zero magnetic field, but it does determine the energy ordering of the symmetric and antisymmetric combinations of the basis states.
[46] Note that in the limit of infinite tunneling rate, which is equivalent to the merger of the two dots, this kinetic exchange splitting becomes the Pauli exclusion principle: The singlet state becomes the only allowed and energetically stable state.
[47] Light-hole states have been neglected.
[48] In principle an optical transition to the T0 triplet could also occur for the higher-energy electron-hole exchange-split state. However, the T0 triplet transition can be expected to be weak because at the resonance the $\uparrow$ electron is tunneling and cannot recombine with the hole ($\Uparrow$). As a result, the overlap integral with the T0 triplet (where the $\uparrow$ electron is not tunneling) is substantially smaller than the overlap integral with the singlet (where the $\uparrow$ is tunneling).
[49] M. Bayer, O. Stern, A. Kuther, and A. Forchel, Phys. Rev. B **61**, 7273 (2000).
[50] Independent values of the electron and hole g factors are determined at electric fields far from any anticrossing region in order to eliminate the impact of resonant changes in the g factor.
[51] G. Salis, Y. Kato, K. Ensslin, D. C. Driscoll, A. C. Gossard, and D. D. Awschalom, Nature (London) **414**, 619 (2001).
[52] M. Poggio, G. M. Steeves, R. C. Myers, N. P. Stern, A. C. Gossard, and D. D. Awschalom, Phys. Rev. B **70**, 121305(R) (2004).
[53] M. J. Snelling, E. Blackwood, C. J. McDonagh, R. T. Harley, and C. T. B. Foxon, Phys. Rev. B **45**, 3922(R) (1992).
[54] J. Levy, Phys. Rev. Lett. **89**, 147902 (2002).
[55] G. Burkard and A. Imamoglu, Phys. Rev. B **74**, 041307(R) (2006).
[56] S. K. Saikin, C. Emary, D. G. Steel, and L. J. Sham, arXiv:0802.1527 (unpublished).
[57] T. Calarco, A. Datta, P. Fedichev, E. Pazy, and P. Zoller, Phys. Rev. A **68**, 012310 (2003).
[58] C. Emary and L. J. Sham, Phys. Rev. B **75**, 125317 (2007).
[59] H. E. Tureci, J. M. Taylor, and A. Imamoglu, Phys. Rev. B **75**, 235313 (2007).
[60] S. E. Economou and T. L. Reinecke (unpublished).
[61] B. D. Gerardot, D. Brunner, P. A. Dalgarno, P. Ohberg, S. Seidl, M. Kroner, K. Karrai, N. G. Stoltz, P. M. Petroff, and R. J. Warburton, Nature (London) **451**, 441 (2008).
[62] D. Heiss, S. Schaeck, H. Huebl, M. Bichler, G. Abstreiter, J. J. Finley, D. V. Bulaev, and D. Loss, Phys. Rev. B **76**, 241306(R) (2007).
[63] K. V. Kavokin, Phys. Rev. B **69**, 075302 (2004).
[64] E. Ivchenko and G. Pikus, *Superlattices and Other Heterostructures* (Springer, Berlin, 1995).